Discharge and Flame Chemistry in Lithium-Ion Battery Vent Gases

Investigations using Breakdown Experiments with Laser-Based Diagnostics

LRCP-246

Julia Lövgren

Supervisor: Elna Heimdal Nilsson
Co-supervisor: Arman Ahamed Subash
Examiner: Joakim Bood

June 2023

LUND
UNIVERSITY

Division of Combustion Physics,
Faculty of Engineering

Populärvetenskaplig sammanfattning

Spänningsmätningar och laserdiagnostik lär oss om brandsäkerhet i batterier

Som du förmodligen känner till är användningen av fossila bränslen som drivmedel till bilar skadlig för både människor och miljö. Istället är elbilar en lösning som många biltillverkare satsar på idag. Volvo Cars har till exempel beslutat att alla bilar som säljs år 2030 ska vara helt eldrivna. Utvecklingen av elbilsbatterier går fort framåt, men i takt med att man utvecklar litium-jonbatterier som rymmer mer och mer energi ökar också säkerhetsriskerna. Vad händer egentligen om en elbil till exempel blir överhettad eller krockar, och antändliga gaser sprids ut i batterisystemet? Hur interagerar dessa gaser med strömmen, spänningen och de elektriska fälten inuti batteriet? Börjar det brinna, och i så fall på vilket sätt? Det är frågor vi har ställt oss i det här projektet.

I studien undersöktes två gasblandningar, som är sammansatta för att likna batterigaser från litium-jonbatterier med litium-järnfosfat (LFP) respektive litium-nickel-kobolt-aluminiumoxid (NCA) som katodmaterial. LFP-gasblandningen består ungefär till hälften av koldioxid och till en tredjedel av vätgas. NCA-gasblandningen består istället av vätgas till drygt 40 % och kolmonoxid till knappt 40 %. Den första frågeställningen som undersöktes handlar om hur de två gasblandningarna beter sig i ett elektriskt fält, närmare bestämt vilken spänning som krävs för att de ska bli elektriskt ledande. Experimentuppställningen bestod av två kopparelektroder som placerades ovanför öppningen till ett rör där gasblandningarna flödar ut. Genom att lägga på spänning över elektroderna formas ett elektriskt fält, som gör att gasen blir elektriskt ledande och elektroner accelereras i riktning från den ena elektroden mot den andra. Den här studien visade att både större avstånd mellan elektroderna och högre flödeshastighet gjorde att det krävdes mer spänning för att detta skulle ske. Det fanns också tecken på att en blandning av gaser kan kräva högre spänning för att börja leda ström än de rena gaser som den består av var för sig. Studier som dessa av hur batterigaserna beter sig kring ström, spänning och elektriska fält kan bland annat hjälpa oss att förstå om gaserna antänds eller inte då de påverkas av batteriets elektriska miljö.

I projektets andra frågeställning låg fokus istället på att förstå hur de två gasblandningarna brinner ifall de antänds. Detta studerades med hjälp av laserdiagnostik. I flammor reagerar bränsle (i det här fallet batterigaser) med syre, och då bildas och förbrukas bland annat hydroxylradikaler. När de bestrålas med laserljus skickar de själva ut ljus med en annan våglängd än den som kommer in. Ljuset från radikalerna registrerades av en kamera med ett filter som tar bort allt utom den våglängd som hydroxylradikalerna sänder ut. På så sätt kunde fördelningen av hydroxylradikaler i flamman avbildas. Ett särskilt spännande resultat från dessa mätningar var att då endast en liten mängd luft fanns tillgänglig till förbränningen så mättes en mindre mängd hydroxylradikaler än då det fanns gott om luft. Men nu undrar du kanske varför det är så spännande – du vet ju redan att det krävs syre vid förbränning, och då är det ju rimligt att det brinner mindre när det finns mindre luft, och att en mindre mängd hydroxylradikaler mäts. Men, studien visade att i fallet med endast lite luft brann gaserna lika livligt som i fallet med mycket luft! Hur kan detta komma sig? Jo, i studien visades även tecken på att de kemiska reaktionerna i fallet med lite luft drevs av väteradikaler istället för hydroxylradikaler. Sådan förbränning kräver inte lika mycket syre som förbränning som drivs av hydroxylradikaler. Tänk dig ett batterisystem i en bil där det finns batterigaser som har börjat brinna. Batterisystemet är ju någorlunda avskärmat från omgivande luft, men den här undersökningen har alltså indikerat att detta kanske inte räcker för att stoppa gaserna från att fortsätta brinna!

Abstract

Due to the environmental impact of fossil fuels, there has been a growing interest in lithium-ion batteries for electric vehicles. However, safety concerns have arisen regarding potential fire hazards associated with the vent gases of these batteries. This work aims to investigate the role of electrical discharge as a proposed ignition source of battery vent gases.

A set of research questions for the study of this newly discovered issue is formulated, and two gas mixtures are selected for this particular work. The chemical compositions of the mixtures represent vent gases from lithium nickel cobalt aluminium oxide (NCA) batteries and lithium iron phosphate (LFP) batteries. An experimental setup is implemented to study the breakdown voltage of these gas mixtures, using gas flow between two electrodes. The impact of gas temperature, flow velocity, chemical composition and electrode separation distance is studied, as current and voltage across the electrodes are recorded. Furthermore, an arrangement for planar laser-induced fluorescence measurements (PLIF) of hydroxyl (OH) radicals is added to the setup, with the purpose of evaluating the flame behaviour following ignition by the discharge. Chemical kinetics simulations are also performed, the trends of which are discussed in relation to the OH PLIF results.

The breakdown voltage of both gas mixtures is found to increase with increasing electrode separation. No firm conclusion can be drawn regarding the effect of temperature, flow velocity or chemical composition, which is attributed to the sensitivity of the setup. The discussion of the results is limited by the lack of literature on breakdown in non-uniform electric fields, which is the case in the present setup. If made more robust, the setup however shows promise to reveal the breakdown characteristics of gas media. The trends of the chemical kinetics simulations can be related to the OH PLIF results. Combined, the simulations and the OH PLIF measurements show that the combustion of gas mixtures at a high fuel-to-air ratio is driven by H radicals. This implies that fire can sustain inside a battery pack despite the absence of oxygen, which is highly relevant for the development of safer electrical vehicle batteries.

Acknowledgements

I thank my supervisors Elna Heimdal Nilsson and Arman Ahamed Subash for providing such an interesting project and for all their support and encouragement during the work. I would especially like to thank Elna for her guidance in the project planning, chemical kinetic analyses and thesis writing. I would especially like to thank Arman for his guidance in the laboratory and for sharing his knowledge about experimental work. I am also grateful to Alexander Petersson, my co-thesis student in this project, for our collaboration.

I thank my co-supervisors Ivan Rexed and Leopold Werberg at Volvo Cars for their support and input along the way of this thesis work.

I thank my examiner Joakim Bood and my opponent Saga Westerberg for their thorough reading of the thesis and their valuable thoughts and questions during the defence.

I thank everyone at the Division of Combustion Physics for including me in your workplace in the best possible way. I especially thank Christian Brackmann, Andreas Ehn, Yupan Bao and Sebastian Nilsson for sharing their expertise in different areas of this project. I also thank the Combustion Kinetics group, I have enjoyed being part of your group this semester. I thank my office mates Isa Hendriks, Love Kildetoft, Klara Lozani Gerdhem and Alexander Petersson for a fun semester.

Lastly, I thank my family, my friends and Sondre Duna Lundemo for their support throughout this thesis work. I am truly lucky to have you.

Contents

1

Introduction and Purpose

1.1 Background and Motivation

This Master's thesis project is part of an ongoing collaboration between Volvo Cars and the Division of Combustion Physics at Lund University, and as such the project aims to serve the purposes of both industry and academia. Volvo Cars emphasize the safety of the vehicles they manufacture, and due to the rapid progress in the development of battery electric vehicles (BEVs), the safety of lithium-ion batteries has become of particular interest. Ultimately, the aim of Volvo Cars is to develop batteries that are safer than the batteries of today, both in normal usage and when exposed to abuse and malfunction. One aspect of this is to prevent battery fire accidents, from occurring due to so-called thermal runaway. Scientists at the Division of Combustion Physics are investigating the chemical and physical properties of various combustion processes. Therefore knowledge, skills and resources are in place that may be used to provide novel input into the thermal runaway issues identified by Volvo Cars. To advance this work, this Master's thesis project serves to gain an understanding of the chemical and physical properties of ignition and reactions in lithium-ion vehicle battery vent gases. This scientific understanding may further on be used by Volvo Cars in developing solutions to the problems on the industry side.

So far, scientists at the Division of Combustion Physics have performed combustion analysis of vent gases from batteries [1, 2], showing that there are likely sources of ignition for battery fires other than heating alone. Volvo Cars representatives believe electrical discharge may be such a source of ignition, but the phenomenon is not well understood. The aim of the Master's thesis project is therefore to identify the scope of the problem and to perform experiments on selected points of particular interest. The work on this problem is currently at an early stage, and identifying and formulating the relevant research questions is therefore part of the thesis work.

The thesis begins in this chapter with a brief review of relevant literature used in combination with discussions with representatives of Volvo Cars and the Division of Combustion Physics to identify the selected problem scope. This review leads to the problem definition, formulated as a series of events with research questions attached to each step. Two of the steps were selected as the focus of this thesis and have been studied in two sets of experiments at the Enoch Thulin laboratory of the Division of Combustion Physics at Lund University. Each of these sets of experiments and the associated background theory is presented in their own chapter, Chapters 2 and 3. Finally, the thesis is finished with the general conclusions of this work and an outlook for future work in Chapter 4.

1.1.1 Lithium Ion Batteries in Electric Vehicles

Electric vehicles (EVs) are rapidly being developed, as a part of the transition to more environmentally friendly options for transportation than previously used. The use of fossil fuels contributes to greenhouse gas emissions causing global warming and other environmental issues. Consequently, avoiding fossil fuels is becoming increasingly urgent. In this context, lithium-ion batteries (LIBs) are pivotal in the transition to EVs, enabling decreased use of fossil fuels for transportation [3]. A battery pack used to run an EV is typically made using hundreds or thousands of battery cells connected to gain more power. This means that large amounts of energy are stored in such a battery system, and also that a safety issue may cause large damage if leading to a fire. There is always a risk of abuse of the batteries in EVs since all vehicles face a risk of for example crashes and overheating. The risk of thermal safety issues regarding batteries is a bottleneck for wider use of EVs [3], and it is therefore urgent that these issues are addressed.

As mentioned, abuse of the conditions that the LIB is designed for may result in a thermal event or thermal runaway, where heat is released to the extent that it ignites surrounding material. Such abuse can be divided into thermal abuse such as overheating and fire exposure, electrical abuse such as overcharge and -discharge and short circuit, and mechanical abuse such as crash, penetration and bend. There can be mechanical abuse such as penetration causing electrical abuse in the form of a short circuit, which in turn causes heating which results in thermal abuse leading to thermal runaway. In other words, the different forms of abuse may together cause a full-blown fire accident [4].

Several attempts have been made to modify the battery materials to avoid thermal runaway, for example, surface coating of the cathode and/or the anode and using flame-retardant or thermal shutdown additives to the electrolyte [5]. It is also relevant to consider countermeasures towards thermal runaway once it is already triggered, such as fire extinguishing and ensuring enough evacuation time for passengers in the vehicle. While heat release from a single cell in thermal runaway is limited, the thermal runaway propagation can cause the release of the considerable amount of energy stored in the full battery pack. In a single cell, the thermal runaway mechanism is driven by chemical reactions while the propagation in the pack is better described in terms of heat transfer. Present research is however not sufficient to establish a mechanism for thermal runaway propagation, and the behaviour may change when more energy is stored in future battery packs [5]. This provides motivation for this thesis work. While there is much more that can be said about lithium-ion batteries, it is left here for the interested reader to further explore. Many reviews have been written on lithium-ion battery failure mechanisms and prevention strategies, for example [6], [7] and [8], in addition to the papers already referenced.

1.1.2 Present Work

This thesis work builds on theoretical investigations of chemical kinetics made by Elna Heimdal Nilsson [1] and an experimental prestudy made by Arman Ahamed Subash [2] at the Division of Combustion Physics at Lund University in 2022, both in collaboration with Volvo Cars. Chemical kinetics simulations were performed on several gas mixtures representative of vent gases from different lithium-ion battery chemistries at different states of charge. The term "vent gases" refers to the gases produced by electrochemical and chemical reactions that take place when the battery is abused or malfunctioning [1]. The simulations indicate that the battery vent gases in themselves are not as prone to ignition as battery tests at Volvo Cars have indicated, which suggests that there is an ignition source present other than solely heating. Testing at Volvo Cars has indicated that electrical discharge could potentially be such an ignition source. This phenomenon is however relatively newly discovered and in need of further investigations, which is how the experimental prestudy [2] along with the idea for this thesis work was born.

Based on [1], two of the gas mixtures were selected and studied in [2]. The same two gas mixtures have been selected for this study, and they are assembled based on lithium nickel cobalt aluminium oxide (NCA) battery chemistries and lithium iron phosphate (LFP) battery chemistries respectively, both at 100% state of charge. The NCA battery cathode material is $Li_x(Ni_{0.8}Co_{0.15}Al_{0.05})O_2$, studied previously in [9, 10]. The LFP battery cathode material is Li_xFePO_4, previously studied in [9, 11]. The molecular composition of the two gas mixtures is shown below in Table 1.1.

	$\mathbf{CO_2}$	**CO**	$\mathbf{H_2}$	$\mathbf{CH_4}$	$\mathbf{C_2H_4}$	$\mathbf{C_2H_6}$
NCA	10	37.1	42.8	7.1	3	0
LFP	48.4	9	29.5	5.6	7	0.5

Table 1.1 Mole fractions of constituent gases in the two gas mixtures studied.

The initial aim of this thesis was to investigate arcing as an ignition source in malfunctioning batteries, however, the specific research questions and methods to answer them were not defined at the beginning of the project. Hence, the thesis work began with a period of literature review as well as discussions with representatives from Volvo Cars and the Division of Combustion Physics at Lund University in order to define the problem and phrase the research questions to investigate within the thesis. The findings of this initial phase of the thesis work is summarized in the following Figure 1.1, where suggested techniques to study parts of the problem are also displayed.

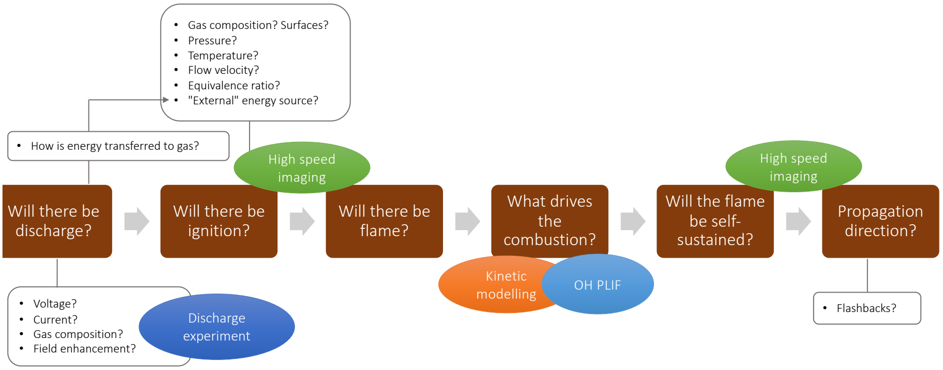

Figure 1.1 The scope of the full problem, including techniques to study it.

In Figure 1.1, the problem is sliced into a chronological series of events. First, there is the question of whether there will be discharge at some given conditions in a battery. Electrical discharge is dependent on several factors, including the amount of voltage and current supplied as well as the medium through which the discharge occurs. The geometry of the surroundings is also a factor, since current running through sharp edges may produce electric field enhancement effects, causing discharge to be more or less likely. Once discharge has occurred comes the question of whether the gases in the battery will ignite from it or not. In order to answer this, one needs to know how what energy would be supplied from the discharge and how this energy would transfer to the gas molecules. What it takes for ignition to occur is of course also dependent on the gas composition, the pressure, the temperature and other aspects. When a thermal event occurs in a battery, the liquid electrolyte evaporates and thus causes pressure buildup and ejection of gas. The flow velocity of this ejected gas also affects the likelihood of it igniting. Since the evaporated electrolyte gases come into contact with surrounding air in and outside the system, the ratio of “fuel” to air also plays a role in the ignition. Once ignition has taken place, there is the question of whether there will be a sustained flame or not, and in that case how it will propagate.

As explained, the scope of the full problem is quite extensive, and this review is meant both to provide context for the selected investigations performed in this thesis and to provide openings for further questions to be investigated in future work. The focus of this thesis work was to design and build an experimental setup to measure both the conditions of discharge and to measure the ignition and combustion phenomena that for certain conditions follow discharge, using high-speed camera and laser diagnostics. Two sets of experiments were made using the resulting setup. First, the breakdown voltage between two electrodes under different battery-relevant conditions (in terms of temperature, flow velocity, gas composition and electrode separation distance) was measured. This experiment was performed together with Alexander Petersson, a fellow Master's thesis student in the project, and is reported both in his thesis and in this one. The work on building and designing the setup was also shared between us. A description of the experimental setup is found in Appendix A and a risk assessment is found in Appendix B, both documents are co-authored by Petersson. The second set of experiments was conducted with the purpose of recording ignition and burning behaviour at different conditions using a high-speed camera and planar laser-induced fluorescence imaging of hydroxyl (OH) radicals. The results from the high-speed camera measurements were obtained and processed by Petersson, and are found in his Master's thesis [12]. The measurements on OH radical distribution using planar laser-induced fluorescence are, together with the breakdown voltage measurements, the focus of the present thesis.

1.2 Scope and Outline of Thesis

The flowchart in Figure 1.1 shows an outline of the chain of events of interest within this project. The full problem consists of several steps, and two of those steps are studied in this work. After the introduction provided here in Chapter 1, these two steps are treated in one chapter each.

The first step selected is the first one shown in Figure 1.1: will there be discharge? The goal here is to understand why discharge may occur in a malfunctioning battery environment, where the gas mixtures mentioned are present together with a high-voltage system. As a first step towards this understanding, a developed version of the setup previously used by [2] is designed, implemented and used to measure the breakdown voltage and current at different conditions. The measurements performed serve both to validate the setup and to gain indications on the conditions affecting whether breakdown occurs or not. This part of the study is described in Chapter 2.

The second step selected from Figure 1.1 is the fourth: what drives the combustion? The goal here is to understand how a flame would behave in each gas mixture upon being ignited by the discharge. This is a question of vast complexity and in this work it is limited to studying the distribution of OH radicals, as an indication of the different zones in the flame where fuel is present and combustion reactions take place. This is done using OH planar laser-induced fluorescence measurements and is described in Chapter 3.

Finally, the conclusions from both experiments are gathered and discussed in an overall conclusion in Chapter 4, along with an outlook to further research.

2

Conditions for Electrical Discharge

In this chapter, gas discharge is investigated as a potential ignition source of battery vent gases. To begin, the objectives of the investigation are stated, followed by a brief review of the mechanisms behind gas discharge relevant to our case. Then follows an account of the experiments performed to investigate the preconditions of discharge formation by measuring the breakdown voltage between two electrodes at different conditions along with the results.

2.1 Objective

The purpose of this set of experiments is to implement and test a setup for the systematic study of breakdown characteristics of gas mixtures, and to use this setup to study the two gas mixtures representing LFP and NCA battery chemistries. Such studies are not found in the literature, so this is to be considered a prestudy of the breakdown voltage and current of each gas mixture along with air, O_2 and N_2. The setup previously used in [2] was further developed and the experiments in this work also serve to validate the new setup and test whether breakdown voltage and current measurements can be made using such a setup. Breakdown voltage and current are measured simultaneously for several electrode separations between 0.25 and 3 mm, and for different conditions in terms of temperature (150°C and 300°C), gas media (LFP, NCA, air, O_2, N_2 and a mixture of 79% N_2 and 21% O_2) and flow velocities (5, 10 and 15 m/s).

2.2 Background

What follows here is a brief introduction to gas discharge and the various types it is commonly categorized as, as well as the physics of the charge production and decay that plays a key role in discharge processes. This is based on the classic textbook by Raizer from 1991 [13] as well as the tutorial and review of the state of the art by Fu et al. from 2020 [14]. After this, some further theory and results of previous work are accounted for regarding discharge in gas mixtures as compared to pure gases.

2.2.1 Gas Discharge

The original explanation of gas discharge was based on the discharge of a capacitor in a circuit with a gas-filled gap between the electrodes. When sufficient voltage or electric field is applied across the gap, the gas is ionized and thus becomes electrically conductive, which allows the capacitor to discharge. The voltage drops and the current increases abruptly. Nowadays the term gas discharge has come to include any flow of electric current through gas ionized by an applied electric field, regardless of the mechanisms behind it.

To begin with, consider two electrodes connected to a DC power supply placed at a distance from each other with some gas medium in between. If a low voltage is applied, no discharge is visible. Charges in the gas medium are produced naturaly by cosmic rays and radioactivity, and when the low voltage is applied they are pulled to the electrodes producing a small current. If the voltage is increased, the current also increases as more charges are pulled to the electrodes instead of recombining, thereby contributing to the current. When the voltage is increased to the point where all naturally occurring charges are pulled to the electrodes, the current saturates as it is limited by the ionization rate in the gas. If the voltage is increased even more, the current spikes and light is emitted. This is referred to as breakdown, and the threshold voltage for this phenomenon is referred to as the breakdown voltage. The process starts with a small number of electrons, whose energy increases as they move with the electric field. When such an electron collides with an atom in the gas along its path, it knocks out another electron and the two electrons continue knocking out even more electrons from other atoms they encounter. This creates an electron avalanche which ionizes the gas, causing the current to grow by several orders of magnitude.

The breakdown voltage is dependent on various factors both in terms of the parameters of the surroundings such as pressure and resistance in the external circuit and in terms of the mechanisms of electron emission and degree of ionization. In his classic textbook [13], Raizer refers to the following major categories of discharge. At low pressure and high resistance in the external circuit, we get glow discharge. It is characterized by low current and the voltage is in the order of hundreds to thousands of volts. The gas between the electrodes is weakly ionized. In glow discharge, the electrons are knocked out from the cold cathode due to impact of positive ions, a process known as secondary emission. At atmospheric level pressure and low resistance of the external circuit, we instead get arc discharge. It is characterized by high current and low voltage, around some tens of volts. At atmospheric pressure, arcs usually form low-temperature plasma. In arc discharge, electrons are emitted from the cathode by thermionic emission, meaning that the cathode is heated up by the current and thereby emits electrons. If the voltage is high enough at around atmospheric pressure, spark discharge occurs. Then a plasma channel rapidly forms between the electrodes, and they are short-circuited. A final category of discharge is corona discharge, which happens when the electric field is nonuniform and cannot cause breakdown of the full gap between the electrodes. Instead, a corona is visible around for example sharp edges of wires at high voltage. The different categories of discharges are also classified as non-self-sustaining and self-sustaining. The most relevant category for the present study is the spark discharge, which is a non-self-sustaining, or transient, type.

2.2.2 Mechanisms of Charge Production and Decay

In the bulk of the discharge, most charge is produced by electrons colliding with atoms and molecules and thereby ionizing them. The number of ionization events per electron per second is called the ionization frequency, ν_i. The ionization frequency is a function of the electron energy distribution function (EEDF) and the ionization cross-section of atoms in their ground state. The ionization frequency of a weakly ionized plasma in an electric field can be found experimentally or by solving the kinetic equation for the EEDF. If the ionization frequency is constant and the removal of electrons by attachment can be neglected, an electron avalanche is formed where the number of electrons n_e increases exponentially with time t,

$$n_e = n_e(0)\mathrm{e}^{\nu_i t}. \tag{2.1}$$

The ionization frequency is key to describing the behaviour of the electron avalanche in time, and to describe it in space the ionization coefficient α is used. The ionization coefficient represents the number of ionization events per electron per centimetre of travel along the field. For planar electrodes at a separation d with an applied voltage V, the number of electrons in the avalanche at a distance x from the cathode is described by

$$N(x) = N_0\mathrm{e}^{\alpha x} \tag{2.2}$$

and the current at the anode is

$$i = eN_0\mathrm{e}^{\alpha d}. \tag{2.3}$$

Electrons are attracted towards the anode, and the positive ions produced in the ionization events are attracted towards the cathode. However, the ions move slower than electrons and therefore accumulate in the gap, causing it to contain positive space charge. Though, at small currents, this space charge does not significantly distort the otherwise uniform electric field from being known as $E = V/d$. Based on the above expressions, the ionization coefficient α can be found by measuring the current i with varying d and plotting $\ln i$ as a function of d for constant E. The slope of the line $\ln i = C + \alpha d$, C being a constant, is the ionization coefficient α [13]. From this realization, the idea of the first set of experiments (Chapter 2) in the present work was formed. Experimental setups similar to the one used in this work are discussed in the next section, but first, some theory is provided regarding breakdown in gas mixtures as compared to pure gases.

2.2.3 Breakdown in Gas Mixtures

So far we have focused on simple cases where the gas consists of one species. This is, however, not the case for the gas mixtures investigated in this study. The critical evaluation of methods for calculating the dielectric strength of gas mixtures by Chantry and Wootton [15] provides a good starting point for our attempts to predict the ionization coefficients of the gas mixtures relevant for us. They describe three principal methods used to predict the dielectric strength of a gas mixture based on the properties of the individual gases the mixture is comprised of. Dielectric strength refers to the ability of a gas to withstand breakdown when electrical stress is applied. This ability is highly dependent on the ability of the gas molecules to attach electrons of different energies and form stable negative ions, which prevents further electron multiplication from electrons ionizing molecules by colliding with them. Breakdown occurs only when the production of electrons from ionization and the loss of electrons by attachment are balanced, in other words when the reduced electric field E/N (E being the electric field and N being the molecular concentration of the gas) is larger than the value $(E/N)^*$, as denoted by Chantry and Wootton, where production and loss are balanced. $(E/N)^*$ is used as a measure of dielectric strength. The probability that an electron will have an ionizing collision per cm of travel in the field direction is given by the ionization coefficient α, and the corresponding probability that it will be attached to a molecule is given by the attachment coefficient η.

For gas mixtures, a phenomenon known as synergism may occur, which means that the dielectric strength of the mixture is greater than that of a linear addition of the dielectric strengths of its constituent species. Most gas mixtures have synergism in the sense that $(E/N)^*$ of the mixture is larger than the weighted sum of the $(E/N)^*$ of the individual gas components, with the weights being the mole fraction of the respective component in the mixture.

Experimental studies of synergism in SF_6 and N_2 gas mixtures have been performed by Hiziroglu et al.[16]. SF_6 has commonly been used for insulating purposes in power systems, but usage is now restricted in many countries due to its greenhouse effect. Therefore interest is growing in studying gases or gas mixtures to replace pure SF_6 with the purpose of insulation. One such alternative is a mixture of SF_6 and N_2, investigated by [16]. Their study concludes that synergy is observed, where the dielectric strength of the mixture is higher than that of the linear combination of the dielectric strength of the component gases. Synergistic effects in SF_6 and N_2 gas mixtures have also been explored by Osmokrović et al. in [17]. SF_6 is an electronegative gas, meaning that it has a tendency to be negatively ionized by capturing free electrons. This causes the amount of free electrons to decrease, thus modulating the discharge process. An increase in electron capture is thereby desirable when discharge is undesirable. Electrons with lower speed and energy spend more time in the vicinity of an electronegative molecule, in other words, the cross-section for electron capture is larger. Lowering the speed of the electrons can be achieved by adding a molecular gas to the electronegative SF_6, since the electrons may then spend energy on exciting rotational and vibrational states of the molecular gas through collisions and thereby lowering their speed. In the case of Osmoković et al. [17] this molecular gas is N_2, which has a positive synergistic effect. In other words, the strength of the mixture against breakdown is higher. However, it should also be noted that too much N_2 would counteract this effect since N_2 molecules are electropositive. This means that they are prone to forming positive ions upon ionization, causing the release of more free electrons.

2.3 Previous Work

In the present work, we aim to gain experimental knowledge of the preconditions for electric breakdown in gas mixtures representative of battery vent gases. A short review of previous work within experimental breakdown voltage measurements for other gases is given in the list below. This list is in no way meant to be exhaustive, but rather to provide some background to motivate our experimental setup.

Hiziroglu et al., 2020 [16]. *Experimental Study of Synergism in N2 and SF6 Gas Mixtures.* Two brass electrodes of diameter 100 mm were placed in a stainless steel chamber. They were shaped according to the Bruce profile and assembled as parallell plates (more on electrode shape will be mentioned further on), and electrically isolated from the grounded test chamber. One of the electrodes was placed on a movable platform to create electrode separations between 1 and 10 mm. The electrodes were polished and cleaned before each measurement series. The gas mixtures studied were produced by adjusting their partial pressure ratios and injected into the chamber after evacuating it down to a pressure of 10^{-5} Torr. The output of the high voltage supply used was variable between 0.5 and 100 kV.

Oettinger et al., 1998 [18]. *Electron drift velocity and Townsend coefficient in DME-based gas mixtures.* Modified pulsed Townsend technique - observed motion of free charges in a homogeneous electric field directly by their induced currents in field-shaping electrodes. A homogeneous electric field was produced by a parallel plate capacitor with electrodes shaped to guarantee that the highest field of the setup is the homogeneous field in the centre and field enhancements from edge effects are avoided. Electrons and ions were produced by ionization in the gas using an Nd:YAG-laser. A 3 ns UV-pulse is focused to produce an ionization cloud of 10 μm diameter and 1 mm length, where the distance and thus the drift length of the cloud to the electrodes can be varied. The charges induce a signal in the anode and the time dependence of this signal is used to derive the drift velocity and the effective Townsend coefficient.

Ledernez et al., 2012 [19]. *Inter-Electrode Distance and Breakdown Voltage in Low Pressure Argon Discharges.* Flat electrodes were used with measures taken to avoid electric field distortion. Voltage was supplied and the current was measured using an electrometer. The applied voltage was ramped up stepwise with a rate of 5 V every two seconds until the current increased in the range of several orders of magnitude.

Zhang et al., 2020 [20]. *Evaluating the Dielectric Strength of Promising SF6 Alternatives by DFT Calculations and DC Breakdown Tests.* Density functional theory (DFT) calculations were made. Breakdown experiments were performed with DC voltage, using ball-to-ball electrodes made from stainless steel with a diameter of 25 mm. The electrode separation was adjustable from 0.25 to 2 mm. The electrodes were polished after each test to keep surface roughness to around 1 µm. Applied voltage was linearly increased with a rate of 1 kV/s until breakdown occurred, and the peak of the breakdown voltage was recorded. The breakdown voltage value was taken as the average of at least ten tests. The electric field under ball-to-ball electrodes is quasi-uniform, so the breakdown voltage is a linear function of pd (pressure times electrode separation).

Nechmi et al., 2017 [21]. *Effective ionization coefficients and limiting field strength of fluoronitriles-CO2 mixtures.* Two aluminum electrodes were placed opposite each other inside a vacuum chamber. They were shaped according to the Bruce profile with a diameter of 100 mm. The electrode separation was adjustable between 2 and 12 mm. The electrodes were polished and the surface roughness was also investigated for “machined” and “blasted” electrodes.

2.4 Experimental Considerations

With the previous review of experiments performed by others in mind, this section includes a few remarks on the setup implemented in the present work. A two electrode setup is used to measure both the voltage across the electrodes and the current running between them when breakdown occurs. Between the electrodes, a gas flow is running at controlled flow velocity. Both the voltage and the current are measured continuously while using a capacitor bank to supply voltage to the electrodes, and the experiment is performed for a range of values of electrode separation. Ideally, plotting the logarithm of the measured current at breakdown as described above would give the ionization coefficient, as a means of quantifying the strength against breakdown of the gas media between the electrodes at different conditions. However, as mentioned previously, the above expressions hold for the case of planar electrodes, since the theory discussed holds for uniform electric fields. In our case, we use electrodes with sharp tips for the sake of being able to control at which point through the gas flow that breakdown occurs. Another benefit of our electrode setup that we will return to in the next chapter of this thesis is that it provides access to send a laser sheet closely above the discharge without being reflected and interrupted by the electrodes. Sharp tips like the ones used in this work are known to cause field enhancement effects, causing the electric field to be distorted and nonuniform.

When two electrodes are placed at a distance from each other, the electrode shape determines the electric field distribution in the gap. An infinite parallel plate capacitor provides an ideal uniform electric field in the gap. For this case, the intensity of the field is given by $E = V/d$, where V is the applied potential difference and d is the distance between the parallel plane infinite electrodes. In reality this is realized using various electrode geometries. A study of different electrode geometries and their breakdown characteristics is done by Gandi et al. [22]. They test the different electrodes with N_2 in the gap and find that out of the plane-parallel, hemispherical, Bruce [23] and Rogowski [24] profiles, the Rogowski profile has the most reliable performance. Another study investigates how well the plane, the Rogowski and the Bruce profiles create a uniform electric field in the gap [25]. This study finds the Bruce profile to be a good choice.

Another aspect of the setup in the present study which complicates matters is that discharge occurs through gas flow rather than in a chamber of still-standing gas. Our interest in the flow aspect of the probability of breakdown stems from the link to the real case - if gases are formed due to electrochemical and chemical reactions in a vehicle battery at thermal runaway, they will not be still standing.

Further on, the theory presented here regarding the ionization coefficient is used as inspiration for the setup and data analysis, even though the additional conditions to this setup make a direct comparison of results to previous works unsuitable. It should also be noted that the additional conditions applied in the present study are part of why the study is interesting, as the motivation is to provide new insight into a less idealized case corresponding to battery-relevant conditions. The current measurements may be used to evaluate how far from the theoretical idealized case the setup is. Regardless of the differences from theory, the dielectric strength may still be evaluated by the experiments as it is measured “directly” in terms of the breakdown voltage.

2.5 Experimental Setup and Procedure

The experimental setup is a further developed version of the one used in [2]. Similar to the setups described in the previous section, this one has two electrodes placed facing each other and a high DC voltage supply connected. Beneath the electrode tips, a quartz tube is placed through which the gas flow is supplied. In [2], the electrodes were placed on a horizontal line and with a fixed separation as shown in Figure 2.1 a). In the present setup, they are instead placed at an angle as shown in Figure 2.1 b), to allow sending a laser sheet directly above the electrode tips as will be described further in the next chapter. The anode is also placed on a translational stage to allow the electrode separation to be changed.

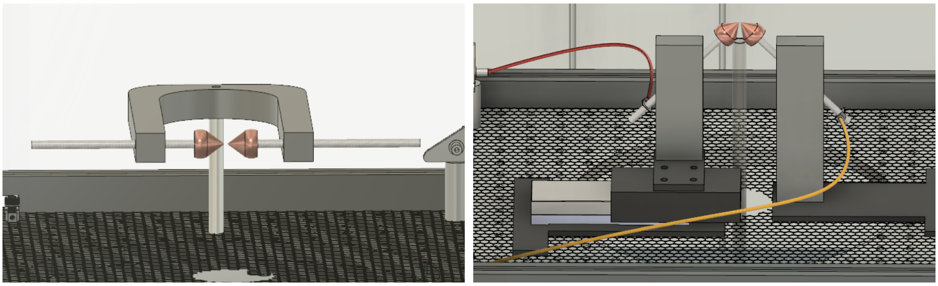

(a) (b)

Figure 2.1 The electrode setup used in [2] (a) and the electrode setup used in the present work (b). Images by Alexander Petersson.

A full description of the electrode setup with dimensions and equipment specifications is found in Appendix A. Figure 2.2 shows a photo of the setup from above.

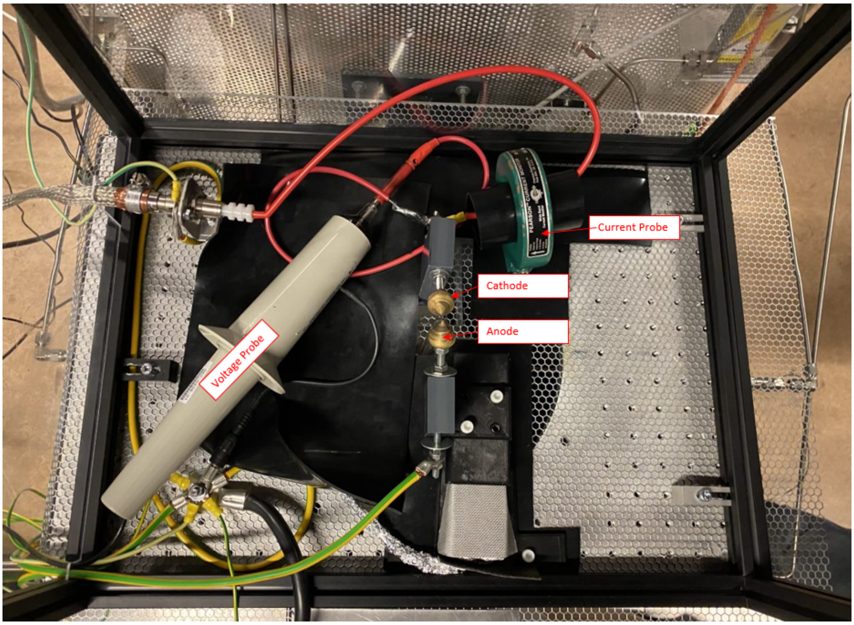

Figure 2.2 The experimental setup showing key parts, photographed from above.

To evaluate the theory regarding discharge in mixtures, measurements of breakdown voltage and current was done in O_2 and N_2 separately and in a mixture of 79% N_2 and 21% O_2. This specific ratio was selected to mimic the composition in air. The idea was to use the current measurements obtained to calculate the ionization coefficient α in the pure gases and in the mixture. The α of the pure gases could then be used as described by the theory to calculate the α of the mixture and compare it with the one measured in the mixture. This would provide knowledge of how the mixing rule would work when having gas flow instead of stationary gas, which is not found in the literature. Validation of the mixture rule would facilitate understanding of how the battery vent gas mixtures work, since the components of them might be better investigated than the mixture and the knowledge on the components could then be useful also with regard to the mixture. Measurements were also made in the still-standing air in the laboratory (no gas flow) and in the two battery vent gas mixtures representing LFP and NCA. To study NCA and LFP, each mixture was supplied in a mixture of 80% N_2 and 20% NCA or LFP respectively. A mixture with a larger fraction of NCA was also tested, but in that case, ignition occurred and measurements were therefore not possible. For this reason, a mixture with 80% N_2 was chosen in measurements of both NCA and LFP in order for the conditions to be the same for the two vent gas mixtures. The purpose of doing measurements in still-standing air is to find indications about whether discharge would occur in a battery high-voltage environment if the vent gases were not present.

In the measurements, the voltage across the electrodes and the current between them were recorded using voltage and current probes respectively (see Figure 2.2). Voltage and current were supplied to the electrodes via a capacitor bank as described in Appendix A. Measurements were made for several electrode separations between 0.25 and 3 mm, and for different conditions in terms of temperature (150°C and 300°C) and flow velocity (5, 10 and 15 m/s) for the gas media mentioned above.

2.6 Results and Discussion

Here the results of the measurements are presented. As mentioned, both voltage and current were measured. Figure 2.3 shows what one acquisition of data looked like. These measurements were made using an oscilloscope (see Appendix A) triggered on the downward slope of the voltage, and Figure 2.3 shows the acquisition made from one trigger event (triggered on the second peak in Figure 2.3 a)). The behaviour seen in this single acquisition is reasonable in relation to theory - the voltage across the electrodes builds up as voltage is supplied by the capacitor bank, and when breakdown occurs the circuit is suddenly closed and current can flow. The voltage then drops rapidly and simultaneously we measure a current spike (see Figure 2.3 b)). As seen in Figure 2.3 a), and more clearly in Figure 2.3 c), for some cases the voltage increases steadily to a certain value, then spikes very rapidly and then drops. The spike was considered an effect of the measurement and not of the breakdown phenomenon, and the breakdown voltage was thus considered the “peak” value before the rapid spike, as shown in Figure 2.3 c). When dropping, the voltage showed oscillating behaviour, which was considered an effect of the measurement and not of importance in relation to the breakdown phenomena. The current spike measured when the voltage dropped has rapid oscillations, as seen in Figure 2.3 d). These are also considered an effect of the measurement.

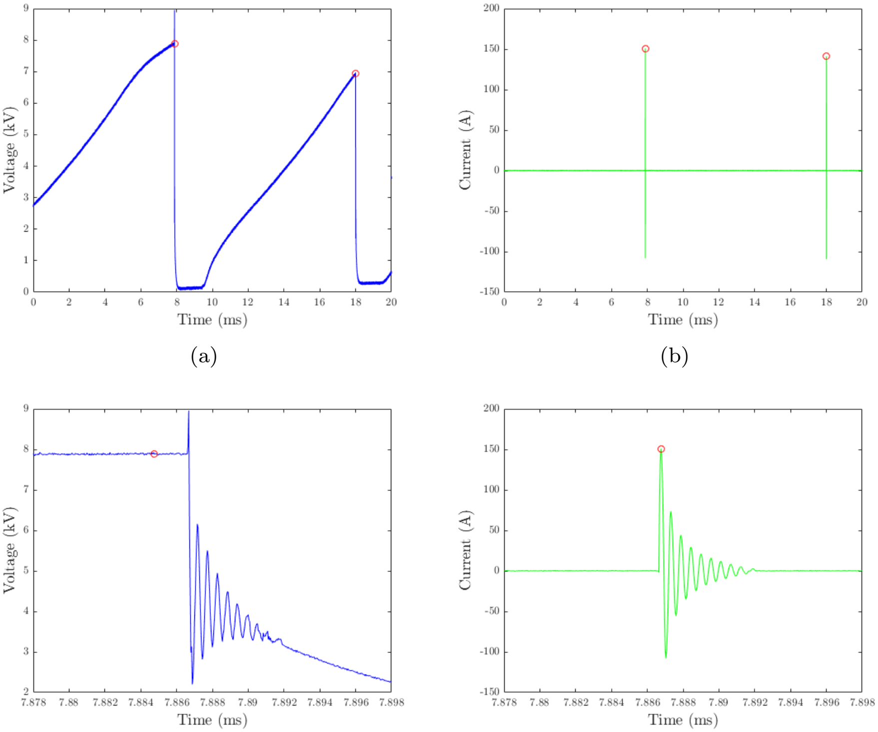

(a)

(b)

(c)

(d)

Figure 2.3 a) Recorded voltage. b) Recorded current. c) Recorded voltage, zoom in on one peak shown in a), to highlight the rapid oscillations and the extra spike at breakdown. d) Zoom in on one peak shown in b), to highlight the rapid oscillations.

Between 50-100 such acquisitions were made with 500 000 data points in each and a time resolution of 40 ns between data points. The identified peaks (marked red in Figure 2.3 a)) were averaged and considered the breakdown voltage for the acquisition series. The same procedure was performed for the current spikes. One such series was performed for each condition and each electrode separation, which results in one value for the breakdown voltage and one for the current at each electrode separation. As seen in Figure 2.3, there can be some variation in the peak heights, mostly for the voltage but also for the current, causing a considerable standard deviation.

As explained previously in section 2.4, the aim was to measure the current for a series of electrode separations and from these data calculate the ionization coefficient if possible. As discussed, it was expected that the results might deviate from the theory, as the theory assumes a uniform electric field which is not the case here due to the electrode shape. The voltage measurements on the other hand give indications directly regarding the dielectric strength. One example of voltage and current measurements is shown in Figure 2.4, to showcase the general behaviour of the data to the reader.

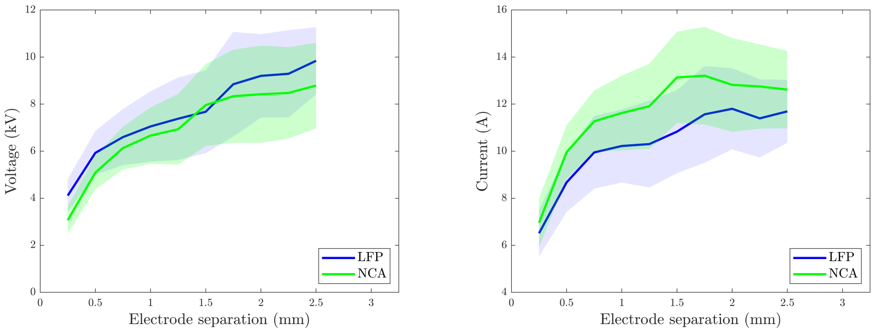

(a)

(b)

Figure 2.4 Breakdown voltage (a) and current (b) for the two battery vent gas mixtures measured at 300°C and a flow velocity of 5 m/s. The calculated values are shown as a line while the shading indicates the calculated value +/- one standard deviation.

In the voltage measurements in Figure 2.4 a), the trend is clear that the breakdown voltage increases when the electrode separation increases. This is reasonable, as there is then more distance in the gas media to be overcome to create an ionization channel. The current measurements shown in Figure 2.4 b), on the other hand, are more difficult to understand in relation to the theory. There seems to be a trend in the breakdown current that it increases with electrode separation to a certain point, and then flattens out or even decreases as the separation increases more. Recall that the theory for a uniform field states that the behaviour should be exponential, to give a linear relation when the current is plotted in a logarithmic scale. Regardless of the physical mechanism behind this discrepancy, the conclusion we make is that the theory and the method described to calculate the ionization coefficient do not hold in this case, probably due to the nonuniform electric field. From now on, we focus on the direct measurements of the breakdown voltage and leave the current plots for the reader to consider in Appendix C.

2.6.1 Varying Temperature

The effect of varying the gas temperature is shown in Figures 2.5 and 2.6. For pure N_2 at a flow velocity of 5 m/s, it can be seen that the values measured for 200 and 300°C are slightly lower than the ones for room temperature (RT) for every electrode separation. Two measurement series were made for N_2 at room temperature performed on different days. These two series show the same upgoing trend but at different voltages. This indicates the sensitivity of the setup, and it is possibly affected by variations in the room temperature. Moreover, there is also a potential effect of the temperature of the electrodes. If the setup had been used immediately prior to the considered measurement, the electrodes could be heated. If the measurement considered was instead the first measurement performed on a certain day, the electrodes could be colder. This requires further testing to be certain. In any case, the difference between the two room temperature series is comparable to the difference between room temperature and higher temperatures, making it uncertain to draw any firm conclusions.

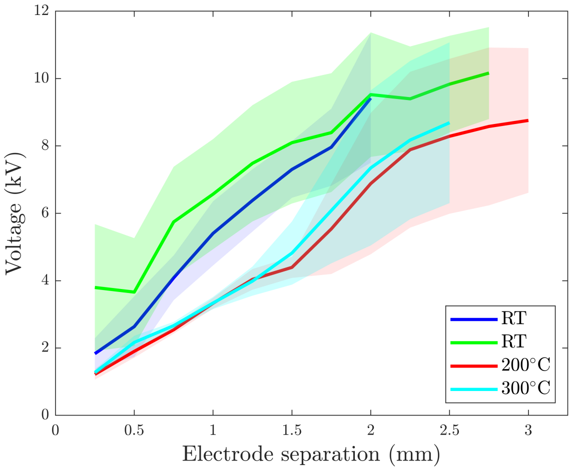

Figure 2.5 Breakdown voltage of N_2 at a flow rate of 5 m/s at room temperature (RT), 200°C and 300°C. Two measurement series at RT are provided.

It is seen in Figure 2.6 that the voltage values for 200 and 300°C are higher than those at room temperature. This is opposite from what we see in Figure 2.5. It seems that temperature has a limited impact on the breakdown voltage in our conditions, but further measurements are required to determine if this is the real case.

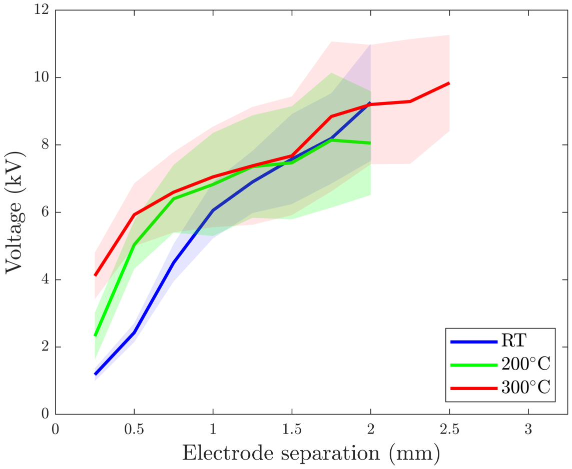

Figure 2.6 Breakdown voltage of the LFP mixture at a flow rate of 5 m/s at room temperature (RT), 200°C and 300°C.

2.6.2 Varying Flow Velocity

The effect on the breakdown voltage of varying flow velocity in room temperature is shown in Figures 2.7 and 2.8. In Figure 2.7, pure N_2 is displayed and no significant difference is visible in the breakdown voltage for the two flow velocities. The same upgoing trend is visible for both flow velocities, in fact one of the measurement series for 5 m/s is almost identical to the one for 2.5 m/s. In Figure 2.8, data is shown for the still standing air in the laboratory along with measurements on a mixture of N_2 and O_2 at air-like proportions (79% and 21% respectively[1]). This measurement series of still-standing air has a much smaller standard deviation throughout, also compared to the measurements shown in the previous Figures 2.5 and 2.6. In Figure 2.8 we see lower breakdown voltage in still-standing air than in 5 m/s of air-like gas flow. It seems reasonable in relation to theory, as the non-zero flow velocity potentially adds transport of charge carriers away from the electrode gap which might cause a higher threshold to form an ionization channel. This however needs further verification, for example with measuring at higher flow velocities to get a more exaggerated difference. It is also worth noting that the still-standing air and the air-like gas mixture are not the same, there are other species in the surrounding air in addition to O_2 and N_2 and there might be particle impurities as well that could affect the breakdown properties.

---

[1] In terms of the volumetric flow velocity, and therefore also in terms of the mole fractions based on the ideal gas law: $PV = nRT \implies V \propto n$, where R is the ideal gas constant, n is the number moles of gas, and pressure P and temperature T are kept constant.

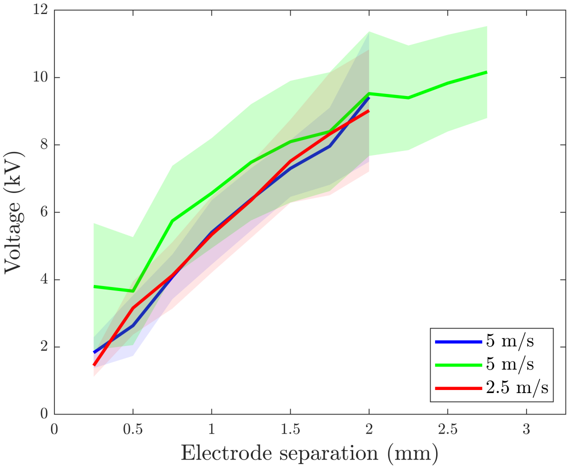

Figure 2.7 Breakdown voltage of pure N_2 at room temperature at flow velocities of 2.5 m/s and 5 m/s. Two measurement series at 5 m/s are provided.

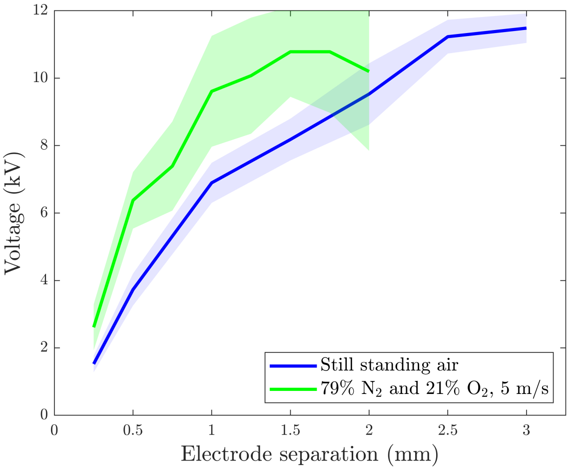

Figure 2.8 Breakdown voltage of the still standing surrounding air in the laboratory and of a mixture of 79% N_2 and 21% O_2 at a flow velocity of 5 m/s, both at room temperature.

2.6.3 Varying Gas Composition

Various gas compositions have been shown already in the previous plots (Figures 2.5-2.8), and a few more figures are included here to showcase the trends. In Figure 2.9, measurements on pure N_2, pure O_2 and a mixture of the two are shown. The breakdown voltage for the pure gases is lower than that of the mixture according to the plot, which could be an indication of synergism as discussed in the theory of this chapter. However, the shaded standard deviations are quite large, making it uncertain to draw such a conclusion from this plot alone.

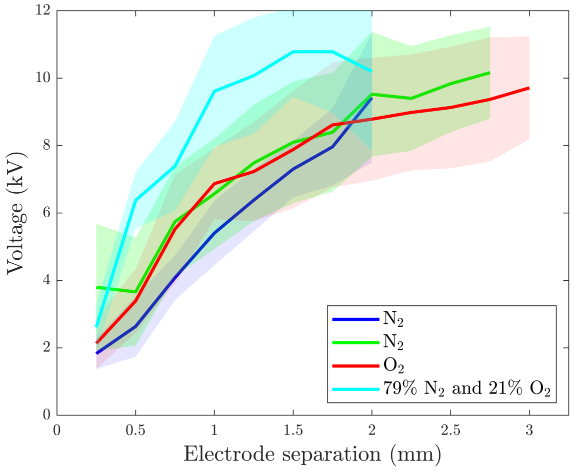

Figure 2.9 N_2, O_2 and a mixture of 79% N_2 and 21% O_2, all at room temperature and with a flow velocity of 5 m/s. Two measurement series are included for N_2.

Figures 2.10 and 2.11 show the results of the two vent gas mixtures LFP and NCA with flow velocity 5 m/s, in room temperature and in 300°C respectively. At room temperature, NCA has a slightly higher breakdown voltage than LFP, while at 300°C we see the opposite. The values are however very close to each other for both temperatures, which indicates either that the difference between these gas mixtures in terms of dielectric strength is very small or that the measurement setup is not sensitive enough to distinguish them.

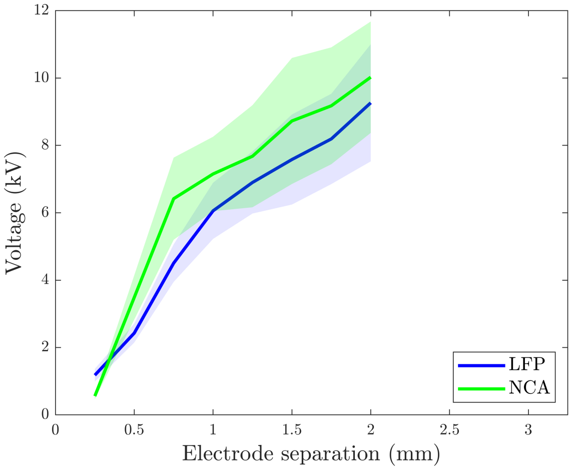

Figure 2.10 Battery vent gas mixtures LFP and NCA at room temperature and flow velocity 5 m/s.

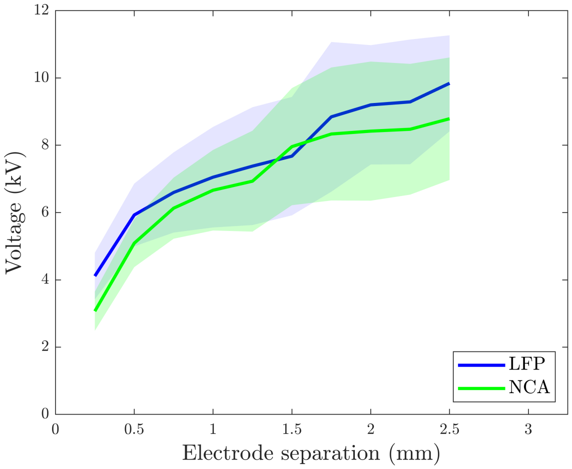

Figure 2.11 Battery vent gas mixtures LFP and NCA at 300°C and flow velocity 5 m/s.

3

Hydroxyl Radical Distribution in Flames

In this chapter, the flame behaviour and chemistry are investigated using laser-based diagnostics, with the goal of exploring what drives the combustion processes in lithium-ion battery vent gases. Laser diagnostics of combustion phenomena have many advantages compared to traditional physical probing. Physical probes intrude in the process they are used to study and may alter the flame behaviour. Moreover, physical probe measurements commonly exhibit poor spatial and temporal resolution. At high temperatures and pressure care also needs to be taken to make the physical probes robust enough, otherwise they are even more likely to perturb the behaviour of the phenomena studied. Laser diagnostics on the other hand are commonly remote and nonintrusive, and in other words, they do not alter the flame behaviour. They allow for measuring temperature and species distributions directly, as opposed to physical probes that need corrections for radiation, convection and conduction within themselves (for example a thermocouple measures its own temperature and not that of the actual gas). Laser diagnostics also allow for high spatial and temporal resolution at the same time [26].

To begin this chapter, some background theory from the literature regarding hydroxyl (OH) radicals in flames is presented, followed by a short review of the planar laser-induced fluorescence (PLIF) technique and structured illumination. Then a description of the experimental setup used to implement the techniques in the present case is given, as well as a description of the post-processing performed. Next, the acquired results are presented and discussed, together with results obtained from kinetic modelling based on [1]. The kinetic modelling was performed in an idealised setting not fully comparable to that of the experiments, and the focus here is placed on trends. The chapter ends with a section regarding methods tested to allow measuring emission from OH radicals in case there is emission in the same wavelength range from the discharge itself.

3.1 Objective

The purpose of this set of experiments is to use the same setup as in the previous chapter with the addition of laser-based diagnostics to investigate the phenomena following discharge causing ignition of the gas mixtures. Measurements are made on the LFP and NCA gas mixtures at two temperatures (150°C and 300°C), three flow velocities (5, 10 and 15 m/s) and several equivalence ratios in the range of $\phi = 0.8$ to $\phi = 4.0$. Chemical kinetics simulations of the radical concentrations and flame speed are also performed using the mechanism provided by [1] to complement the results of the OH PLIF. These represent an idealized scenario and we use only the trends shown in them together with the OH PLIF results to give indications about what drives the combustion in the gas mixtures studied.

3.2 Background

3.2.1 H_2 and CO Oxidation and Radical Chemistry

The following description covering the basics of the relevant flame chemistry is based on the textbook *Combustion* by Glassman, Yetter and Glumac [27]. A flame can be described as a self-sustaining chemical reaction in a discrete reaction zone. Consider a flame anchored at the outlet of a tube with a gas flow of fuel gas running through it. Surrounding air will also be entrained into the tube by the fuel as it enters the tube. The flame is called premixed if the fuel and air (oxidizer) are homogeneously mixed prior to ignition at the outlet, which is the case if the tube is long enough for the air and fuel to mix properly. The flame is said to be laminar if the flow in the tube is laminar. For laminar flow, the flow velocity across the tube is parabolic, with the maximum velocity in the centre of the tube and lower velocity close to the walls. The low flow velocity together with heat loss to the rim of the outlet of the tube causes the flame to stabilize there - the flame is said to be anchored at the outlet.

Such a laminar premixed flame as considered before has a distinct structure, as shown in Figure 3.1 (left). When the flow through the tube is only consisting of fuel, instead of premixed fuel and oxidizer, the flame is a diffusion flame, as shown in Figure 3.1 (right). Then, reactions take place in regions where the fuel meets the surrounding air, with a channel of only fuel in between. The dark zones in the figure consist of unburned premixed gas and the reaction zones are where a large part of the combustion reaction and heat release occurs. The colour of the reaction zone changes depending on the chemistry involved and varies depending on the fuel-to-air ratio. Fuel to air ratio is commonly specified in terms of the equivalence ratio ϕ, defined as the fuel-to-oxidizer ratio in the system divided by the fuel-to-oxidizer ratio at complete stoichiometric combustion. Stoichiometric combustion refers to the condition where the number of fuel and oxidizer molecules is balanced so that all reactants are consumed. If there is more than the stoichiometric amount of fuel, $\phi > 1$ and the system is said to be fuel rich. If on the other hand, there is more oxidizer than the stoichiometric amount, $\phi < 1$ and the system is said to be fuel lean. In a lean hydrocarbon flame, the luminous reaction zone is purple due to emission from excited CH radicals. In a rich hydrocarbon flame, the luminous reaction zone is instead green because of emission from excited C_2 molecules. This illustrative example of the impact of radical chemistry on flame behaviour brings us over to review further theory on flame chemistry.

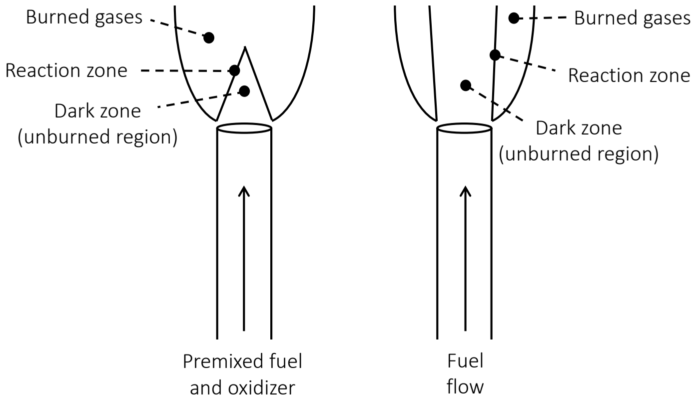

Figure 3.1 Schematic structure of a laminar premixed flame (left) and a diffusion flame (right), inspired by [27].

The gas mixtures studied in this work are, as described previously, inspired by the two battery chemistries LFP and NCA. The LFP gas mixture consists of 48.4 % CO_2 and 29.5 % H_2, while the NCA gas mixture consists of 42.8 % H_2 and 37.1 % CO (see Table 1.1). With this in mind, the focus here will be placed on the chemistry of H_2 and CO in flames. CO_2 is a common combustion product and does not participate in radical-forming reactions. We begin with the chemistry of hydrogen (H_2) flames in air. Such flames are nearly invisible to the human eye, but considerable emission from OH is seen in the UV range. The burned gas consists of about 95-97 % water and the remaining share includes H, O and OH radicals. In the combustion reaction, the initiation step provides the first radical for a system of chain reactions to continue. In this case, the most probable initiation step is (3.1) which provides an H radical, which in turn proceeds with the following reactions (3.2)-(3.5),

$$\mathrm{H_2 + O_2 \longrightarrow HO_2 + H} \tag{3.1}$$

$$\mathrm{H + O_2 \longrightarrow O + OH} \tag{3.2}$$

$$\mathrm{O + H_2 \longrightarrow H + OH} \tag{3.3}$$

$$\mathrm{H_2 + OH \longrightarrow H_2O + H} \tag{3.4}$$

$$O + H_2O \longrightarrow OH + OH \tag{3.5}$$

causing an amount of OH, O and H radicals.

Carbon monoxide (CO) is oxidized quicker if hydrogen is also present, which is the case in our gas mixtures. This is referred to as oxidation in wet conditions. The reaction procedure catalyzed by H_2 is represented by the following reactions

$$CO + O_2 \longrightarrow CO_2 + O \tag{3.6}$$

$$O + H_2O \longrightarrow OH + OH \tag{3.7}$$

$$O + H_2 \longrightarrow H + OH \tag{3.8}$$

$$H_2 + OH \longrightarrow H_2O + H \tag{3.9}$$

$$CO + OH \longrightarrow CO_2 + H \tag{3.10}$$

$$H + O_2 \longrightarrow OH + O \tag{3.11}$$

leading to the formation of OH, O and H radicals. We see that wet CO oxidation involves the reactions already presented for H_2 oxidation, in addition to some steps involving carbon (C). The rate of H_2 oxidation is strongly dependent on the concentration of H radicals, and the rate of CO oxidation is in addition to H also dependent on the concentration of OH radicals. The CO conversion to CO_2 is strongly exothermic and is responsible for much of the heat release in combustion processes.

As mentioned before, the gas mixtures in this study consist mainly of CO_2, H_2 and CO. The other constituents are CH_4, C_2H_4 and C_2H_6, which are all hydrocarbons. Without going into detail regarding the oxidation of hydrocarbons, it is worth noting that this process also generates and consumes OH, O and H radicals.

Finally, some notes regarding the spatial distribution of OH radicals in the different zones of the flame, as OH is the selected radical species to measure in this work. Typically, high OH concentrations are detected in the flame reaction zone where most combustion reactions take place, while a lower concentration is also found in the regions of burned fuel (the post-flame zone). In the unburned regions, there are no OH radicals [28].

3.2.2 Laser-Induced Fluorescence

Now, on to the laser-based diagnostic technique employed to study the previously described combustion processes. The intensity of a spectral line is proportional to the transition probability between two energy states in an atom or molecule. The transition probability is dependent on the wave functions of the energy states, providing the possibility of using intensity measurements as indications of the distribution of excited electrons. The wavelength of the transition, i.e. of the spectral line, provides information regarding the energy levels of the atom or molecule that is of interest [29]. This may also be used reversely - given that the wavelength of a transition in a certain molecule is known, detection of this wavelength will provide information regarding the presence of the molecule in a sample. This is how we utilize it in the present work. Here laser-induced fluorescence is used to detect the most important combustion radical in our case, OH.

Laser-induced fluorescence (LIF) is a technique where the species studied absorbs photons from laser light, inducing spontaneous emission. The emission, i.e. the LIF signal, can be measured perpendicular to the laser beam, thus providing spatial resolution. By expanding the exciting laser beam into a sheet and using a two-dimensional detector, a two-dimensional signal is received. In this case, the technique is referred to as planar laser-induced fluorescence (PLIF) [30]. Several species can be measured, and in the present case we use PLIF to measure the presence of OH radicals.

In this thesis work, OH is excited by a laser sheet at 283 nm through the $Q_1(8)$ transition. This is the transition $A^2\Sigma^+(\nu' = 1) \longleftarrow X^2\Pi(\nu'' = 0)$. Following ground excitation by the laser sheet, vibrational energy transfer occurs from the excited state to the $A^2\Sigma^+(\nu' = 0)$ level, from where the transition back to the $X^2\Pi(\nu'' = 0)$ level occurs. The transition $X^2\Pi(\nu'' = 0) \longleftarrow A^2\Sigma^+(\nu' = 0)$ corresponds to an emitted wavelength of 308 nm [31]. A schematic of the excitation and emission used in PLIF measurements in this work is shown in Figure 3.2.

3.2.3 Structured Illumination

In our use of OH PLIF, the goal is to visualize in two dimensions the OH distribution in the flame. However, electrical discharge is used in our setup to ignite the gas. Then an applied electric field causes the gas between two electrodes to be ionized, which also may produce strong emission across multiple wavelengths. A key difficulty in optical diagnostics in such cases is the interference of the background signals (plasma discharge) with the desired signal [31]. To work around this in our experiments and distinguish the OH signals from the discharge emission we use structured illumination. This codes a pattern into the resulting image so that the signals are separable in the Fourier domain, as further explained below. The technique is called Structured Laser Illumination Planar Imaging (SLIPI) [32], where a sinusoid pattern is coded into the laser sheet causing the laser-induced signal to be modulated. The background signal from the discharge remains unmodulated.

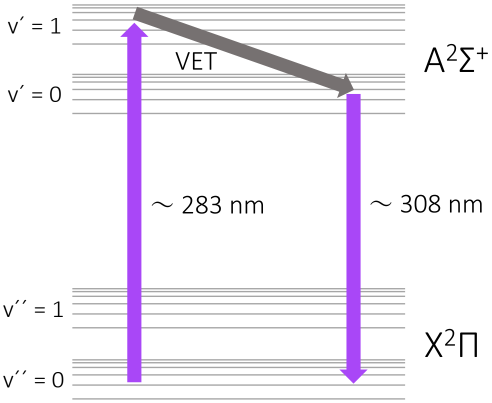

Figure 3.2 A schematic energy level diagram of OH LIF. VET stands for vibrational energy transfer and the levels for each vibrational state v represent different rotational states. The schematic is based on one in [31].

To understand the image coding, we begin with a brief explanation of the Fourier transform of images. Two dimensional Fourier transform $(F(\nu, v))$ and inverse Fourier transform $(f(x, y)$ are used to transform functions between space domain and spatial frequency domain, as given by equations (3.12) and (3.13) below.

$$F(\nu, v) = \int_{-\infty}^{\infty} \int_{-\infty}^{\infty} f(x, y) \mathrm{e}^{-2\pi \mathrm{i}(\nu x + v y)} \, \mathrm{d}x \mathrm{d}y \tag{3.12}$$

$$f(x, y) = \int_{-\infty}^{\infty} \int_{-\infty}^{\infty} F(\nu, v) \mathrm{e}^{2\pi \mathrm{i}(\nu x + v y)} \, \mathrm{d}\nu \mathrm{d}v \tag{3.13}$$

$F(\nu, v)$ is a function depending on the spatial frequencies ν and v while $f(x, y)$ depends on the spatial variables x and y. An unmodulated image transfers to a central "dot" in the Fourier domain, as shown in Figure 3.3 a), while a sinusoid pattern transfers to a "dot" separated from the centre, as shown in Figure 3.3 b) [31]. An unmodulated image and a sinusoid pattern added together transfer to a combination of the separate components in the Fourier domain, as shown in Figure 3.3 c). As is seen in the figure, the modulated and the unmodulated images are separable in the Fourier domain.

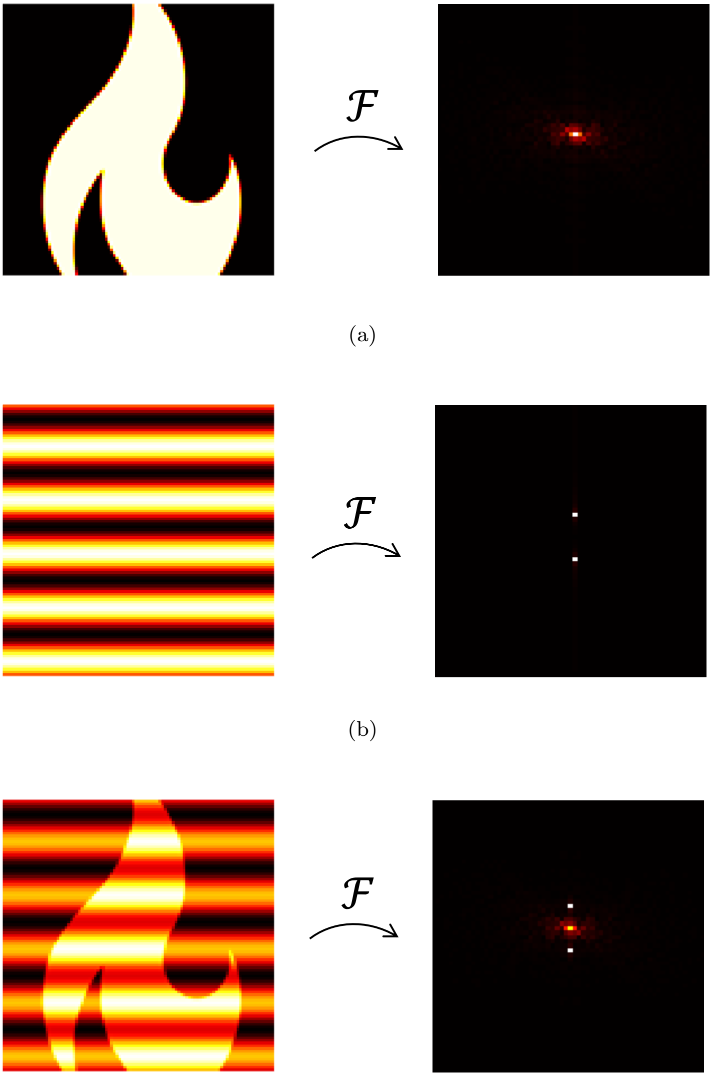

(a)

(b)

(c)

Figure 3.3 a) An unmodulated image (left) and its Fourier transform (right). b) A sinusoid pattern (left) and its Fourier transform (right). c) The images in a) and b) added together (left), and its Fourier transform (right).

3.3 Experimental Setup and Procedure

The experimental setup for this part is the same as referenced before (Appendix A), with the addition of laser diagnostics. A high-speed camera was also used, however, the setup and results from high-speed imaging are the subject of the Master thesis by Alexander Petersson and will not be discussed further in this work with the exception of including some illustrative examples. The setup apart from the laser diagnostics is described in Appendix A, and the addition of the laser setup is described here. The instruments used for OH PLIF include a combination of Nd:YAG and dye laser, a camera to detect the OH PLIF signal and optical elements to create a sinusoidally modulated laser sheet focused in the flame region. A schematic of the setup is shown in Figure 3.4.

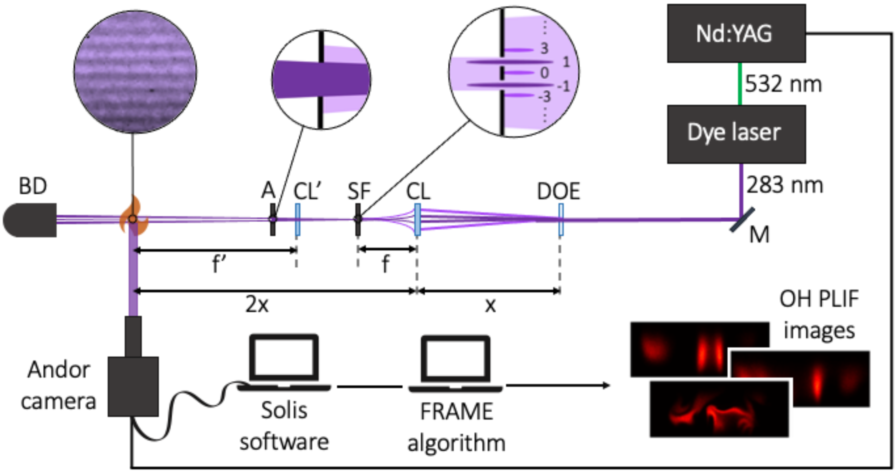

Figure 3.4 Setup for OH PLIF measurements. The graphic representation is inspired by [33]. DOE - diffractive optical element, CL - horizontally oriented positive cylindrical lens ($f = 150$ mm), CL′ - vertically oriented positive cylindrical lens ($f' = 400$ mm), SF - spatial filter, A - aperture, BD - beam dump, M - mirror. Distance $x = 360$ mm.

The following description of the experimental laser setup corresponds to the above schematic (Figure 3.4), and the abbreviations given in parenthesis upon introducing the various components refer to the ones given in the figure. An Nd:YAG laser is used to supply laser light at 532 nm for the pumping of a dye laser. The Nd:YAG unit includes a frequency doubling unit to get 532 nm from the otherwise 1064 nm laser light coming from the Nd:YAG rod cavity. The dye laser uses Rhodamine 6G with ethanol and supplies pulse energy of 14-16 mJ, pulse duration of 10 ns and repetition rate of 10 Hz to generate UV laser light at 283 nm. The 283 nm laser beam is then directed by mirrors (M) into the optics to form a laser sheet and to spatially modulate the sheet with a sinusoidal pattern as mentioned before.

First, the beam enters a diffractive optical element (DOE). It works similarly to a grating, splitting the beam into lines by diffraction. The interference of the two first orders of the diffraction pattern will produce a perfect sinusoid pattern in the light when imaged on the target. However, the interference of the 0th and higher orders cause disturbance to this pattern and it is thus desirable to remove these lines [31]. The 0th-order and the higher-order lines are filtered out by placing a spatial filter (SF) in the focus plane of a positive cylindrical lens (CL, $f = 150$ mm). The spatial filter has two slits as shown in Figure 3.4, only allowing the two first-order components to pass. The DOE used in our experiment has approximately 87% of its energy in the two first orders of the diffraction pattern, with the purpose of avoiding excessive intensity loss when filtering out the other orders. Next, the laser beam is directed through a second positive cylindrical lens (CL$'$, $f' = 400$) oriented vertically that focuses the laser in the horizontal direction, forming a sheet at the target. The sheet then passes through an aperture (A) to preserve only the part of the laser sheet with the highest intensity. Finally, the laser sheet passes through the flame at the target and into a beam dump (BD).

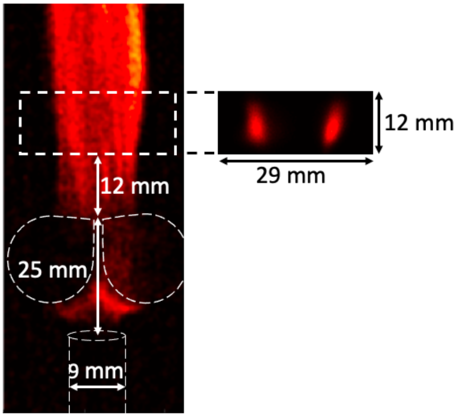

Figure 3.5 The acquisition region for OH PLIF. The dimensions of the acquisition window is shown to the right and apply to all images presented in the results section of this chapter. Other relevant dimensions of the electrode setup are indicated on a single-frame image to the left taken from the high-speed images in [12].

In the flame, the 283 nm laser light excites OH radicals as described previously. The resulting laser-induced fluorescence was recorded perpendicular to the incident laser sheet using an Andor iStar Intensified sCMOS camera at a frame rate of 10 Hz. An image showing the spatial dimensions of the region where data acquisition was made is shown in Figure 3.5, in relation to the high-speed images recorded at the same time as described in the Master thesis by Petersson [12]. A UV filter was placed in front of the camera objective to filter out all wavelengths except the laser-induced fluorescence signal from the OH radicals. The camera was synchronized with the Nd:YAG laser in order to acquire data at the same time as a laser pulse was emitted. The data was acquired using Andor Solis software and post-processed in Matlab as described in the next section.

Data was acquired for several sets of parameter values. The two gas mixtures NCA and LFP were studied at two temperatures (150°C and 300°C), three flow velocities (5, 10 and 15 m/s) and varying equivalence ratios in the range of $\phi = 0.8$ to $\phi = 4.0$. For some cases, data was recorded both for only the flame sustaining after ignition by electrical discharge and for the flame with discharge occurring continuously during the acquisition. For the former case, no plasma is present and all signal measured is therefore coming from OH radicals formed in the combustion reactions. For the latter case, there may also be emission from the plasma included in the signal.

3.4 Data Processing

All recorded images were analyzed and images are presented here for each case in the form of three single shots (generally frame number 40-42) and one average image. The average image is one way to include information from multiple single shots in one, but for some cases with rapid variation in time it might not provide all information, hence the series of three single shots. For all cases except one, 200 frames were acquired and averaged for the average image. For one case, it was for safety reasons not possible to record for the time it took to record 200 frames since flashback occurred, and in this case, only 10 frames were acquired and averaged. The data from the camera was stored and processed in Matlab as matrices with elements representing the intensity recorded for each pixel. Background noise was recorded and subtracted from each image, simply using matrix subtraction. An example of a background-corrected single shot and the corresponding background-corrected average image is shown in Figure 3.6, note the striped pattern on the images from the sinusoidal modulation.

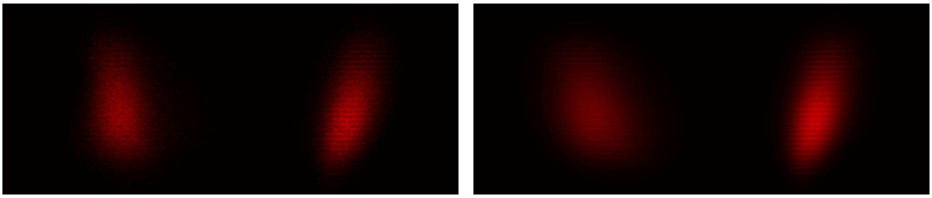

(a) Single frame.

(b) Average image.

Figure 3.6 Background corrected data.

After background correction, the images are passed through a lock-in algorithm. The lock-in algorithm is used to extract the modulated signal based on the known modulation frequency. The structured illumination patterns are separated from unmodulated light in the Fourier domain as described earlier and the modulation frequency is found in the Fourier domain. The code used in this study performs the Fourier transform of the images by fast Fourier transform (FFT). A low-pass filter is placed surrounding the desired signal in the Fourier domain. Typically, in this technique, the filter would be placed surrounding the modulated signal in order to keep it and discard the unmodulated components. However, during data evaluation, it was discovered that the sinusoidal structure imposed in our laser sheet was not sufficiently clear in the recorded data to acquire all the information of the modulated signal from the Fourier domain. Since the structure in the laser sheet was smeared, PLIF signal is found in the unmodulated component as well as in the modulated component in the Fourier domain. Therefore, only the unmodulated component in the Fourier domain was considered for the cases where the signal was not affected by discharge emission. This is discussed in detail in Section 3.6.

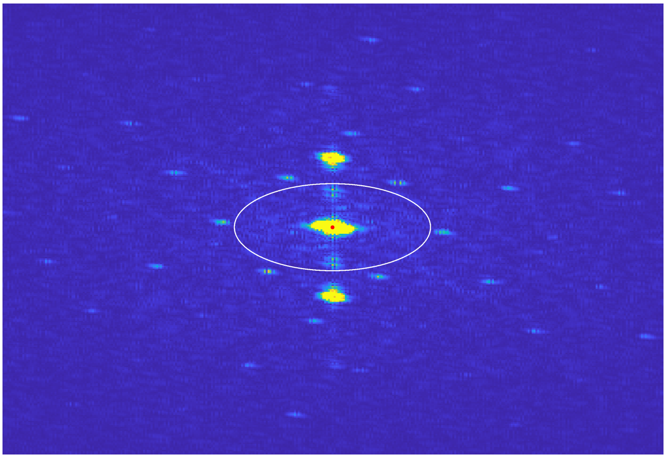

Figure 3.7 Average image in Fourier domain with filter.

A suitable location and size of the filter were determined to be an ellipse with its centre at (641, 326), the length of the semi-minor axis being 30 pixels and the semi-major axis being 65 pixels. As shown in Figure 3.7 this filter is as large as possible without including the high-frequency components, enabling the best possible spatial resolution in the extracted signal. Once the low-pass filter is applied the signal is extracted by inverse fast Fourier transform (iFFT). A mathematical description of the lock-in algorithm in two dimensions used in this study is given in [31]. Further details regarding the lock-in algorithm are given in [34]. The implementation of the lock-in algorithm used in this study was provided by Yupan

Bao at the Division of Combustion Physics, Lund University.[1] An example of an extracted single shot and an average image is shown in Figure 3.8.

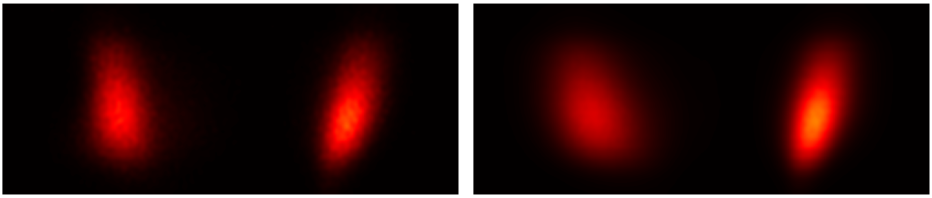

(a) Single-shot.

(b) Average image of 200 single-shots.

Figure 3.8 Background corrected data.

3.5 Results and Discussion

The results from the OH PLIF measurements are displayed here in the form of average images as well as three consecutive single-shots for selected cases, acquired 100 ms apart. Results are presented in two sections beginning with observations regarding the effect of equivalence ratio ϕ on OH distribution, followed by observations of the effect of flow velocity. In both sections, comparisons are made between the two gas mixtures representing LFP and NCA and between the temperatures 150°C and 300°C.

3.5.1 Varying Equivalence Ratio ϕ, Gas Mixture and Temperature

In Figure 3.9, average OH PLIF images are shown for a series of equivalence ratios ϕ.

---

[1] Yupan Bao, personal communication, April 2023. Credit to the FRAME research group.

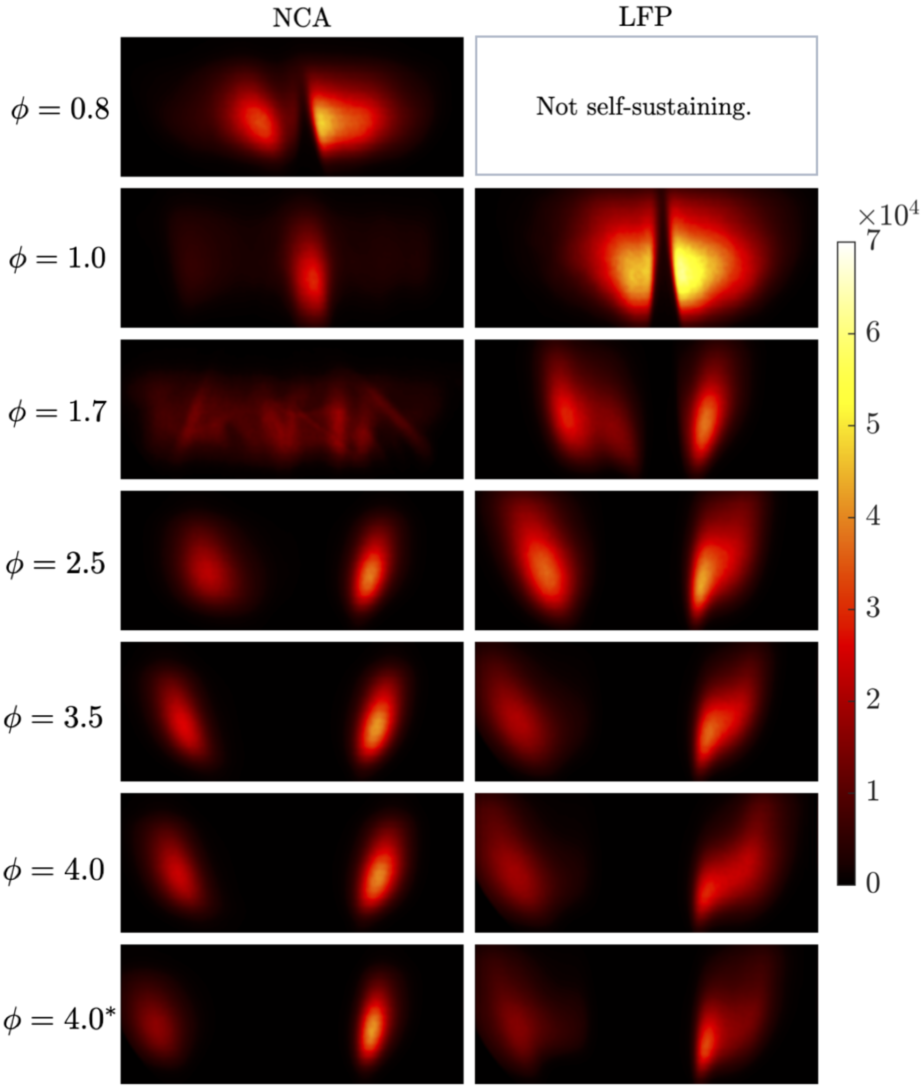

Figure 3.9 Average images, all at 300°C and 5 m/s. The image for NCA at $\phi = 1.7$ is an average of only 10 images, as for safety reasons the recording could not continue for the usual 200 frames. The colour bar shows intensity in arbitrary units.

In Figure 3.9, it is seen that for NCA, there is a clear cone shape in the centre of the image for $\phi = 0.8$. However, for $\phi = 1.0$ and $\phi = 1.7$, the structure is quite irregular, especially for $\phi = 1.7$. For $\phi = 1.0$ the flame was anchored at the outlet of the quartz tube while for $\phi = 1.7$ the flame propagated upstream into the tube. This was observed when performing the experiments and in the high-speed images of [12]. Such flame behaviour is rapid, occurring at time scales shorter than the frame rate of the OH PLIF acquisitions. Therefore, the average image gives an unrepresentative picture and the phenomenon is better understood from the series of single-shots displayed in Figure 3.10. For $\phi = 2.5$ and above we see two regions with OH signal some distance apart. The distance between them increases with an increasing equivalence ratio. This is attributed to the increase in fuel flow and the expansion of the non-reacting fuel-rich area in the centre. Case $\phi = 4.0^{*}$ shows the same conditions as for $\phi = 4.0$ but with the oxygen supply cut off. This case was included to show the characteristics of a known diffusion flame, as the only oxidizer available then is that which diffuses into the fuel mixture after the outlet of the quartz tube. By comparing to the $\phi = 4.0^{*}$ case it can be stated that for all rich cases ($\phi > 1$) for the LFP mixture, and for cases with $\phi > 1.7$ for NCA, the flame shows diffusion flame behaviour. The flame is sustained only in the form of two regions where the oxygen in the surrounding air mixes with the fuel-rich mixture to attain the flammability limit. The results for this case are very similar to those for $\phi = 4.0$, indicating that there is a diffusion flame also at $\phi = 4.0$.

For LFP, the flame was not sustained for $\phi = 0.8$, and therefore no measurement could not be made. This is reasonable as it is a lean case with a fuel mixture containing a high concentration of CO_2. For $\phi = 1.0$ a cone shape in the centre of the image is observed, similar to the case of NCA at $\phi = 0.8$. Such a cone shape is indicative of a premixed laminar flame as shown in Figure 3.1. For $\phi = 1.7$ the flame behaviour is sustained in the form of two regions in a diffusion flame-like manner. For $\phi = 2.5$ and above the behaviour is similar to that for NCA, namely two regions with OH signal. The distance between them is similar to the distance in the NCA cases and also increases with increasing equivalence ratio. The same remark regarding the $\phi = 4.0^{*}$ case compared to the $\phi = 4.0$ case for NCA is valid for LFP.

In Figure 3.11, average images are shown for three selected values for the equivalence ratio from the previously studied range, this time at 150°C. These images show similar features as the 300°C cases. The average images for $\phi = 1.0$ and $\phi = 1.7$ for NCA have a smeared-out structure, indicative of a turbulent flame and flashback as mentioned previously. The latter case, as well as $\phi = 1.7$ for LFP, are shown as single shots in Figure 3.10, which provide a complementary representation of the phenomena. In LFP at $\phi = 1.0$, there is a cone shape structure indicative of a premixed flame, while at $\phi = 1.7$, there are two regions of signal. This is reasonable as for the latter case there is a richer fuel mixture, causing the cone to be elongated into a dark channel. For LFP at $\phi = 3.5$, the fuel mixture is even richer and the reaction takes place in a diffusion-like manner. For $\phi = 3.5$ both the NCA and LFP gas mixture show similar regions of OH signal as they do for 300°C. There is not a clear difference in intensity between corresponding

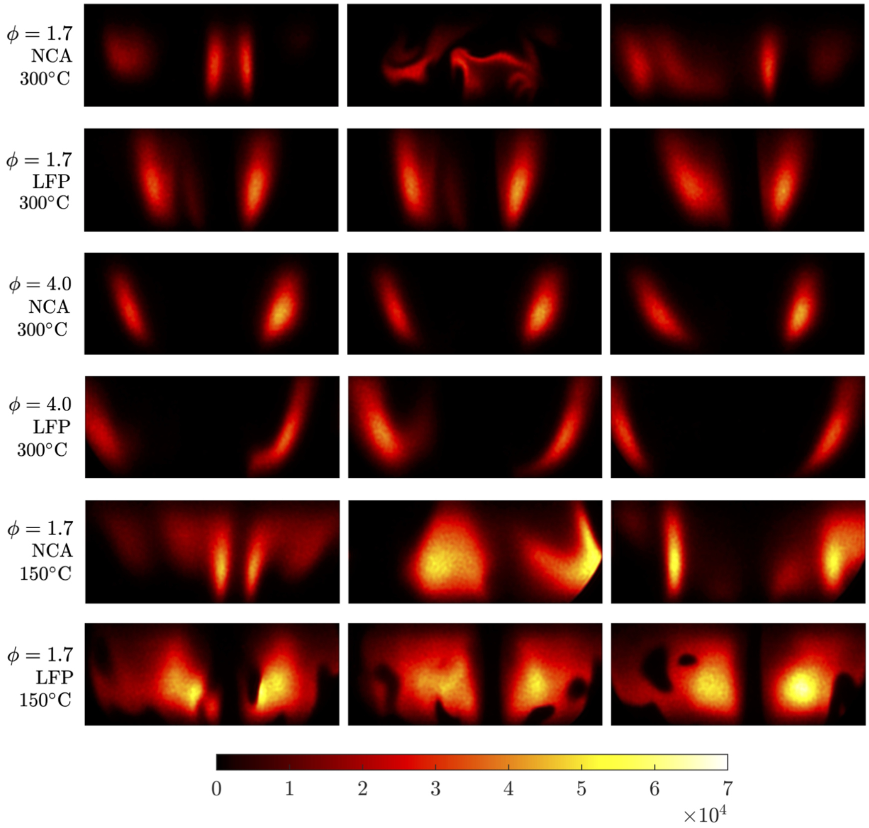

Figure 3.10 Single-shot images, each row showing a sequence of three images taken 100 ms apart for the conditions given to the left. All are taken at a flow velocity of 5 m/s. The colour bar shows intensity in arbitrary units.

cases at different temperatures, but there are other aspects that differ. In LFP at $\phi = 1.0$, the centre cone is elongated downstream for 300°C compared to 150°C. As heat was supplied after the flow velocities had been set, the temperature does not affect the mass flow. It does however affect the actual flow speed at the outlet as a higher temperature causes the volume to expand, and thereby increases the flow speed. This explains why the tip of the cone is further downstream at the higher temperature than at the lower.

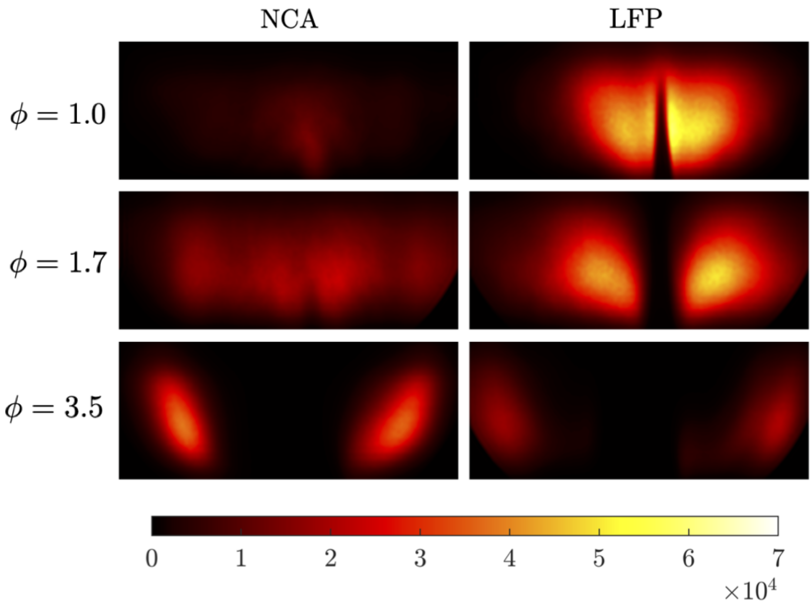

Figure 3.11 Average images, all at 150°C and 5 m/s. The colour bar shows intensity in arbitrary units.

3.5.2 Varying Flow Velocity, Gas Mixture and Temperature

Now we look at the results where the flow velocity was varied. Results taken at equivalence ratio $\phi = 1.0$ with the NCA gas mixture are shown in Figure 3.12 in the form of average images. The signal is much stronger for the two higher velocities than the lowest. The flame structure also appears more turbulent, as seen in the single shots presented for 10 and 15 m/s in Figure 3.13, causing the smeared look of the average images in Figure 3.12. The trend in behaviour is consistent between the two temperatures. It can be noted however that both for increasing temperature and for increasing the flow velocity, the tip of the center cone moves downstream. This is reasonable in terms of higher mass flow velocity. In regard to the temperature, it is also explainable but might require a bit more thought. Since heat is supplied after the flow velocity values are set, the different temperatures still have the same mass flow. A higher temperature does however cause the volume of the gas to expand, causing a higher actual flow speed at the outlet which explains the tip of the cone moving downstream.

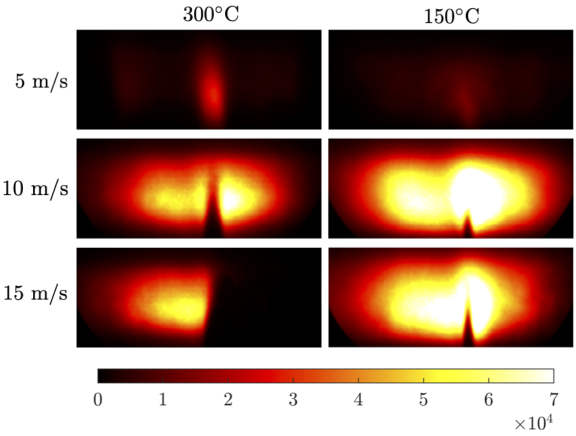

Figure 3.12 Average images of NCA at $\phi = 1.0$. The colour bar shows intensity in arbitrary units.

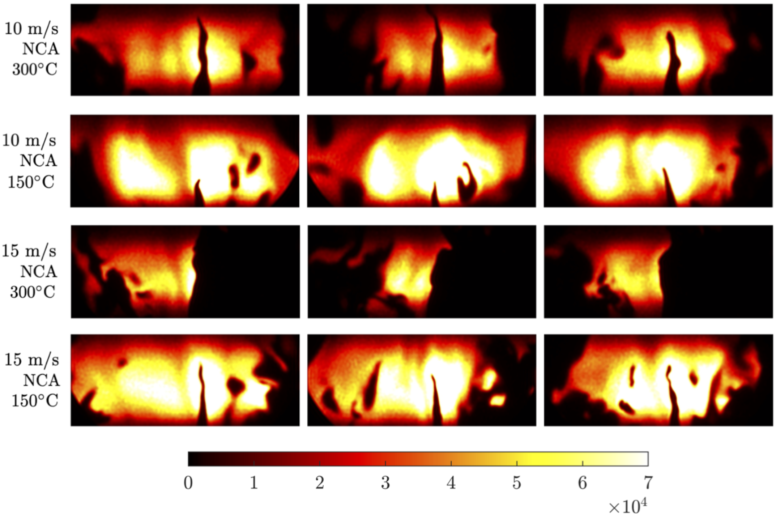

Figure 3.13 Single shots taken at $\phi = 1.0$. The colour bar shows intensity in arbitrary units.

The top two images in Figure 3.12 can be recognized from Figure 3.9 and Figure 3.11 respectively. Both these flames had flashback behaviour. For 10 m/s and 15 m/s however, the flame was self-sustained and propagating downstream in a turbulent manner. In the bottom left image, corresponding to a flow velocity of 15 m/s at a temperature of 300°C, there is only OH PLIF signal on one side. This could be due to the flame anchoring on this side only. It may be noted that Figure 3.12 only shows data for NCA. LFP was also studied, but the flame was not self-sustained for 10 or 15 m/s at either temperature. The results for LFP at $\phi = 1.0$ have been shown previously in Figures 3.9 (300°C) and 3.11 (150°C) respectively.

For equivalence ratio $\phi = 3.5$ as seen as average images in Figures 3.14 (300°C) and 3.15 (150°C), the behaviour was quite similar for the two temperatures. One exception is that at 300°C the LFP did not produce a self-sustained flame at 15 m/s and $\phi = 3.5$, while at 150°C it did. These two figures at $\phi = 3.5$ are quite different from Figure 3.12 at $\phi = 1.0$, which is reasonable given the trend in flame behaviour shown in the previous section on the impact of equivalence ratio (Figures 3.9 and 3.11). For $\phi = 3.5$ at flow velocity 5 m/s, both gas mixtures show two regions with OH signal at both temperatures. The regions are sharper for NCA than for LFP in the average images, indicating less fluctuations in time. Furthermore, there seems to be a trend for LFP at both temperatures for the two regions of OH signal to be less separated as the flow velocity increases. In both gas mixtures, the regions with OH signal also become smudged in the average images as the flow velocity increases. This is better observed in the single shot sequences shown in Figure 3.16, which show that the regions with OH signal look more turbulent for higher flow velocities than for lower and also more turbulent for LFP than for NCA.

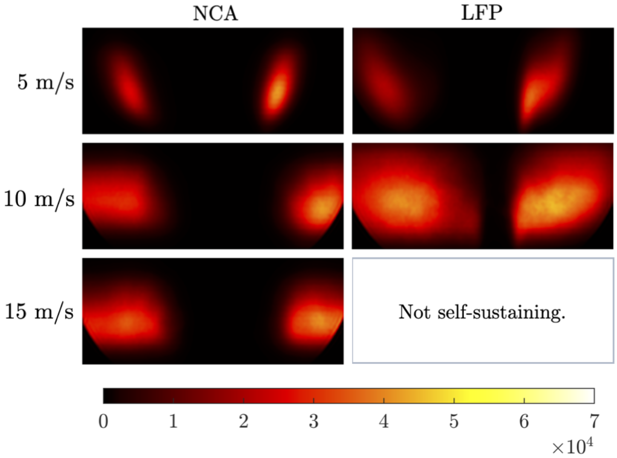

Figure 3.14 Average images at $\phi = 3.5, 300°\text{C}$. The colour bar shows intensity in arbitrary units.

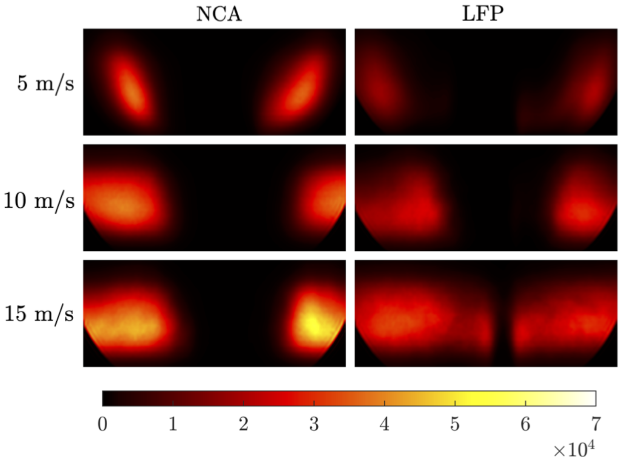

Figure 3.15 Average images at $\phi = 3.5, 150°\text{C}$. The colour bar shows intensity in arbitrary units.

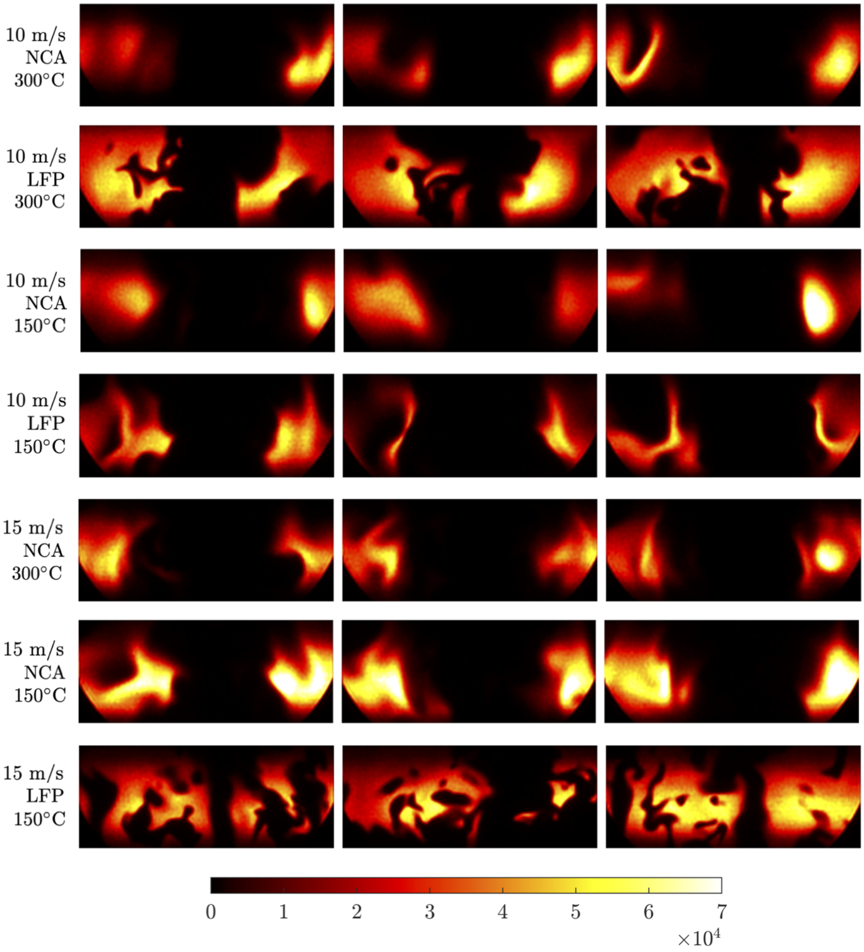

Figure 3.16 Single shots taken at $\phi = 3.5$. The colour bar shows intensity in arbitrary units.

3.5.3 Chemical Kinetics Modeling in Relation to Experimental Results

Chemical kinetics modelling was performed in the software Chemkin [35], using the mechanism in [1] to extend the results on flame speed and radical concentration previously simulated. In this work the simulations for LFP and NCA were extended to higher equivalence ratios (now up to $\phi = 4.8$ as compared to around 2 in [1]) and with the additional temperature of 300°C (only 150°C in [1]).

In Figure 3.17, simulation results of flame speed are shown. We see that the trends are similar at both temperatures, but the flame speeds are much higher at 300°C compared to 150°C.

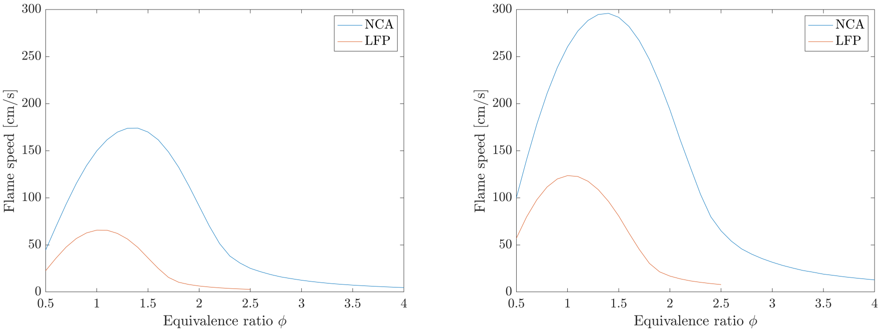

(a)

(b)

Figure 3.17 Simulated flame speed of LFP and NCA at different equivalence ratios, for 150°C (a) and 300°C (b).

In Figure 3.18, the relative concentrations (mole fraction of each radical divided by total radical concentration) of O, H and OH radicals are shown at 150°C and 300°C for the two battery vent gas mixtures. In Figure 3.19, the absolute mole fractions of O, H and OH radicals are shown at 150°C and 300°C. When looking at the relative concentrations in Figure 3.18, the trends are the same at both temperatures and overall similar between the two gas mixtures. When looking at the absolute mole fractions in Figure 3.19, it is evident that the concentrations are much lower for LFP than for NCA, and much lower at 150°C than at 300°C. This is well in agreement with theory, as the concentration of reactive species in LFP is lower than in NCA since it consists to a large part of CO_2 and as higher temperature enables faster reactions.

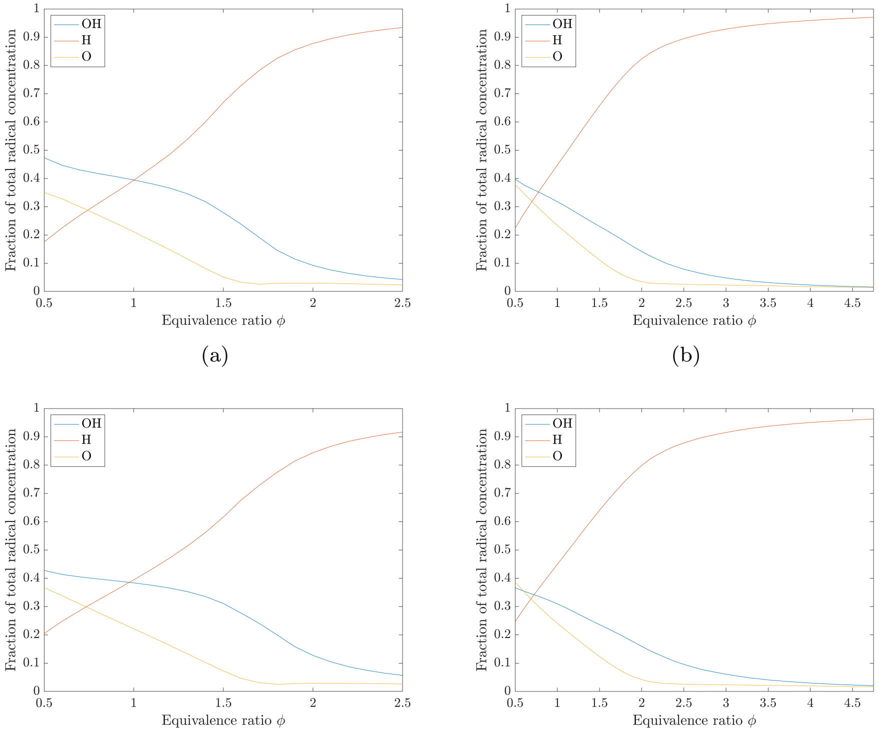

(a) (b)

(c) (d)

Figure 3.18 Relative concentrations (mole fraction of radical X divided by total radical concentration) of O, H and OH at different equivalence ratios are shown. Simulations are performed at a temperature of 150°C for LFP (a) and NCA (b), and of 300°C for LFP (c) and NCA (d). For LFP, only $\phi \leq 2.5$ are shown since the flame speed simulations showed that a flame was not sustained above this point.

Combined together, the simulations and OH PLIF results provide interesting insight. It should be noted, however, that the simulations were conducted within a highly idealized framework. Among various assumptions, a laminar premixed flame is assumed. As seen in the previous OH PLIF images, this is not always the case. Hence, when discussing the simulations and the experiments relative to each other, we only look at the trends. At high equivalence ratios, both the OH PLIF images shown previously (Figures 3.9 and 3.11) and the simulated radical concentrations indicate lower amounts of OH than at low equivalence ratios. Moreover, the simulated flame speeds in Figure 3.17 indicate that there is still a sustained flame, which is also in agreement with what was observed in the experiment when looking at the visible flame and in the high-speed images taken simultaneously as the OH PLIF measurements.

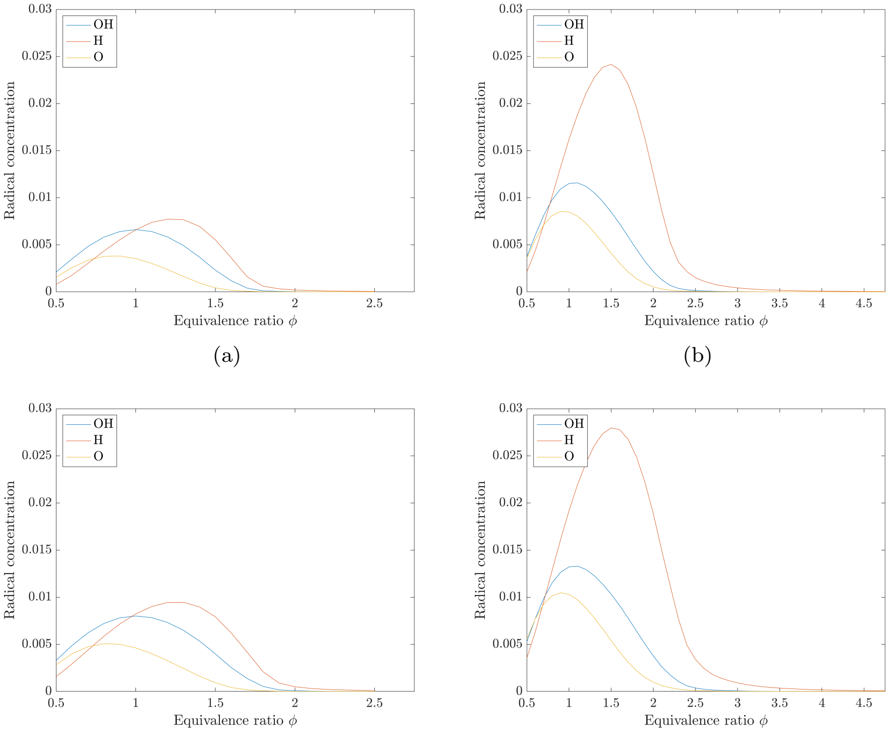

(a)

(b)

(c)

(d)

Figure 3.19 Absolute mole fractions of O, H and OH at different equivalence ratios are shown. Simulations are performed at a temperature of 150°C for LFP (a) and NCA (b), and of 300°C for LFP (c) and NCA (d). For LFP, only $\phi \leq 2.5$ are shown since the flame speed simulations showed that a flame was not sustained above this point.

An average image of the flame from the high-speed images in [12] is included here in Figure 3.20, along with the corresponding OH PLIF image, to demonstrate this. In Figure 3.18, it is clear that as the equivalence ratio increases, H radicals form the vast majority of the radical pool present. All results combined, there are indications that the combustion at fuel-rich conditions is driven by hydrogen combustion.

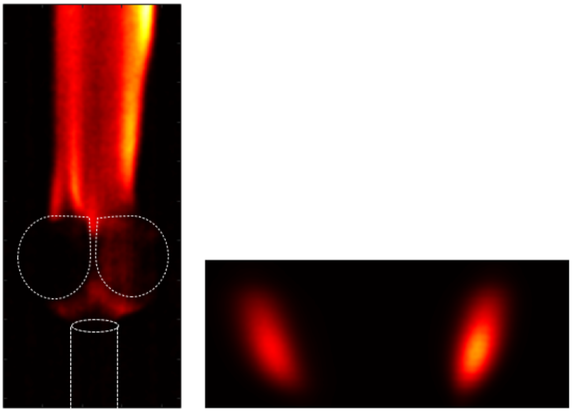
(a) (b)

Figure 3.20 Average image of the flame in NCA at 300°C, 5 m/s and $\phi = 3.5$ taken with a high-speed camera at a frame rate of 10 kHz (a) and the corresponding OH PLIF average image (b). The high-speed image is an average of 300 single shots, and the OH PLIF image is an average of 200 single shots.

3.6 Impact of Discharge - Method, Results and Discussion

As mentioned before, apart from the main OH PLIF measurements that were recorded after the discharge was turned off there were also some measurements made when the discharge was continuously sparking. The purpose of this was to examine whether the discharge would emit light in the same wavelength range as the OH radicals in the combustion reactions, and in that case investigate if structured illumination could be used to distinguish between these two signals. The resulting images from this investigation are presented here. In the images presented so far, the unmodulated signal was extracted by the lock-in algorithm. Now we look at both the unmodulated and the modulated parts of the signal. The modulated part of the signal was extracted using the same method as described previously, but now placing the filter around the higher frequency part of the signal as shown in Figure 3.21. A suitable filter, in this case, was determined to be an ellipse with its centre at (641, 280), the length of the semi-minor axis being 10 pixels and the semi-major axis being 15 pixels.

An image of the sinusoidally modulated laser sheet used is shown in Figure 3.22, where one can see that parts of the sheet exhibit quite poor structure. This affects the ability to extract the modulated signal correctly, which will be seen in the upcoming results.

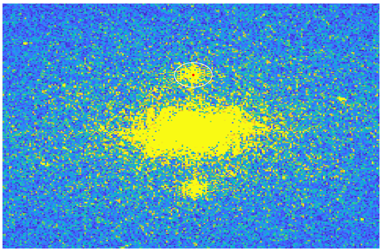

Figure 3.21 Average image in Fourier domain with filter.

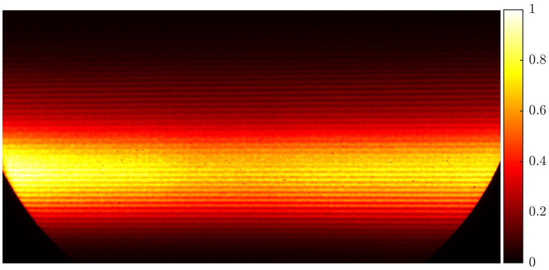

Figure 3.22 Laser sheet in air shown with normalized intensity.

Figures 3.23 and 3.24 present data for both gas mixtures at $\phi = 1.0$ and flow velocity 10 m/s, using the unmodulated and the modulated signal respectively. The same is shown in Figures 3.25 and 3.26 but with $\phi = 3.5$. When presenting the data, different scales of the intensity colour bars are used for the unmodulated and modulated images. The signal intensity for the modulated part was significantly lower than the one for the unmodulated, so a reduced maximum intensity of the colour bar was necessary to visualize the signal. In both figures showing the modulated part, a stripe of lower intensity is visible across the centre. This is due to the signal not being extracted properly as the modulation pattern was not distinct enough in this part of the laser sheet, as previously shown in Figure 3.22. Despite this issue with the modulation, the same structure of the flame is visible in the images with and without modulation. This indicates that there is no emission from the discharge in the same part of the spectrum as the emission from the OH radicals, and also that the procedure for extracting the OH signal would work well if the modulation pattern was clearer. There could still be emission from the discharge in other wavelength ranges that are filtered out by the UV filter on the camera in our case. If PLIF is done using different species than OH with emission wavelengths closer to the emission of the discharge, the setup described and tested here, including structured light, could be useful to separate the emission from the selected species in the combustion reactions from that of the discharge.

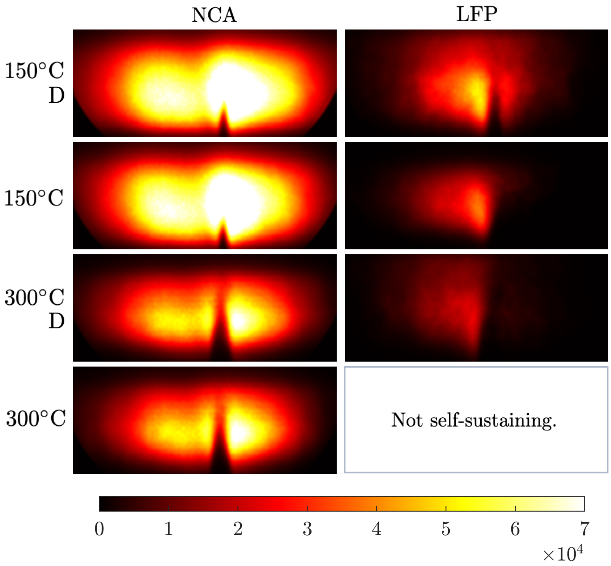

Figure 3.23 $\phi = 1.0$ and 10 m/s, unmodulated part. The colour bar shows intensity in arbitrary units.

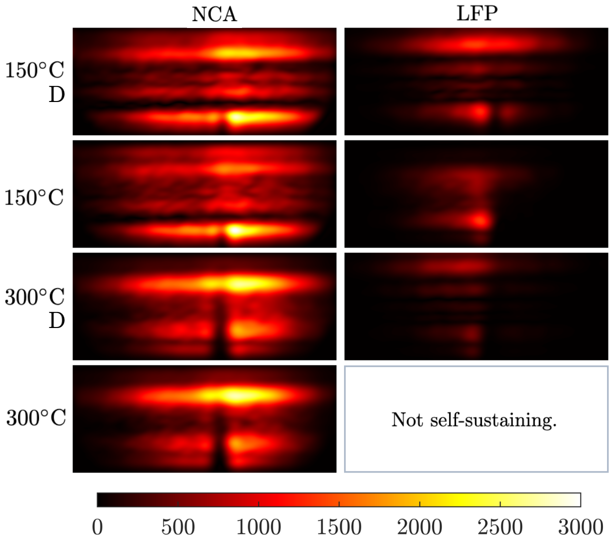

Figure 3.24 $\phi = 1.0$ and 10 m/s, modulated part. The colour bar shows intensity in arbitrary units.

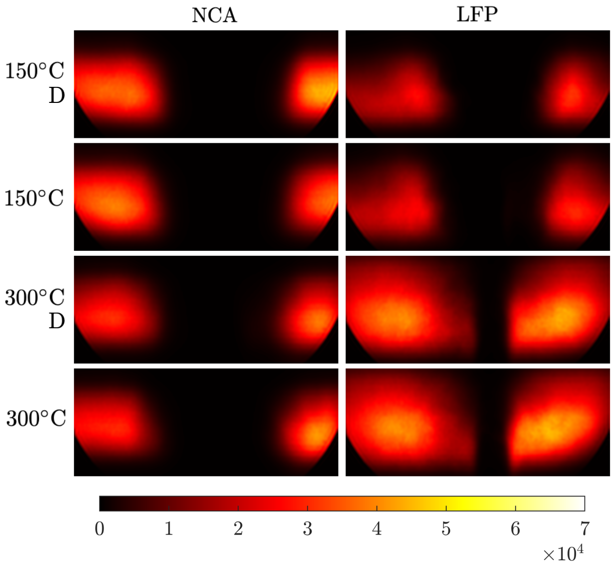

Figure 3.25 $\phi = 3.5$ and 10 m/s, unmodulated part. The colour bar shows intensity in arbitrary units.

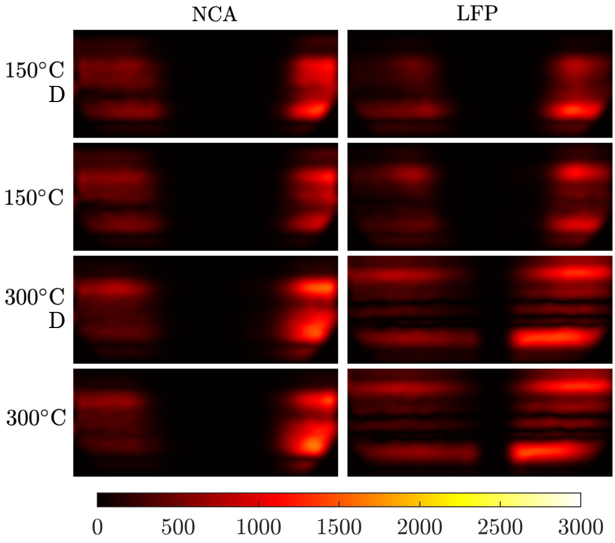

Figure 3.26 $\phi = 3.5$ and 10 m/s, modulated part. The colour bar shows intensity in arbitrary units.

4

Conclusions and Outlook

This chapter begins with a summary of the results and discussions of each of the two experimental studies. Following this, some final conclusions and an outlook to further research are given, both with regard to the particular experiments performed in this work and to the lithium-ion vehicle battery research field.

4.1 Conditions for Electrical Discharge

In all measurements, it was observed that the breakdown voltage increases with an increase in electrode separation. The reason could be that there is then a larger amount of gas to ionize in order for breakdown to occur. The electric field across the electrodes is also affected by distance. Regarding the current measurements, an exponential relation between current and electrode separation would be expected if the field was uniform. However, the field in our case was not uniform and, indeed, we could not identify the characteristic behaviour predicted by theory. The measurements were performed to investigate whether there were signs of these characteristics in spite of the failing assumption of a uniform field. The conclusion is that no such behaviour was found.

The experimental setup was found to be very sensitive. This is seen for instance in the measurements of N_2 at different temperatures, where the two measurement series at room temperature were found to differ from each other by an amount comparable to the difference between those at 200°C and 300°C. The results, however, still show indications that temperature might not affect the breakdown voltage to a large extent.

Furthermore, the results showed some indication that higher flow velocity gives higher breakdown voltage, potentially explained by charge carriers being transported away from the electrodes by the flow and thus not contributing further to the ionization process. There is also an indication of synergism in the mixture of O_2 and N_2, as seen when comparing the breakdown voltage of the separate gases and of the mixture. This is in agreement with the presented theory. No significant difference was observed in the breakdown voltage of LFP compared to NCA.

4.2 Hydroxyl Radical Distribution in Flames

For lean flames (low equivalence ratio), behaviour corresponding to a premixed flame is observed. In these cases, a cone of no OH PLIF signal was observed, corresponding to the unburned fuel. For rich flames (high equivalence ratio), diffusion-like flames were instead observed. In these cases, there were two regions of OH PLIF signal with a channel of no signal in between. The distance between the two regions of signal (width of the channel) was increasing with an increasing equivalence ratio. These observations are in agreement with the well-studied behaviour of premixed and diffusion flames.

For the different temperatures considered (150 and 300°C) it was observed that for higher temperature and lean conditions, the cone structure was elongated downstream. This can be understood by the fact that the heat causes the volume of the gas to expand. This gives a higher volumetric flow speed even though the mass flow speed is the same, and the increased volumetric flow elongates the unburned fuel region. It was also observed in the cases where the flow velocity was varied while other parameters were kept invariant. Higher flow speed resulted in an elongated cone of unburned fuel, and in some cases even in diffusion-like behaviour of the flame.

The simulation results indicated that an increase in the equivalence ratio leads to a decrease in the amount of OH and O radicals, while the concentration of H radicals increases. OH radicals dominate at lean conditions, while H dominates at rich. For cases when a low OH PLIF signal is observed and low OH concentration is seen in the simulation results, the simulated flame speed results still indicate a sustained flame. This indicates that the combustion at rich conditions is indeed driven by H radical formation and consumption, as the simulation results suggest.

Finally, a remark on the OH PLIF measurements performed with continuous discharge and post-processed using the sinusoidally modulated signal. These results indicate that there is no emission from the discharge in the same wavelength range as the laser-induced fluorescence from OH. In further OH PLIF measurements with the same setup used in this work, it is therefore not necessary to use structured illumination to distinguish discharge emission from the OH radicals involved in the flame reactions. If other species are measured and thereby other spectral lines are used, there might however be discharge emission in the same wavelength range as the PLIF wavelength. In this case, the structured illumination setup used in the present work could be a useful approach.

4.3 Conclusion and Outlook

It is necessary for the setup for breakdown voltage measurements to be more stable to enable reproducible results. The setup could benefit strongly from a more controlled environment, both in terms of temperature and pressure. One could for example monitor the temperature of the electrode tips, to account for the temperature effect on thermionic emission of electrons. Another approach could be to wait a considerable time between measurements to ensure that the electrodes have cooled. It would also be interesting to measure and control the surface roughness of the electrodes, as that might affect the likelihood of breakdown by locally distorting the electric field.

It would be interesting to perform similar breakdown voltage and current measurements using electrodes with a profile made to produce a uniform electric field. This could reduce the effect of the geometry parameter and thus provide insight into the gas medium alone. Such knowledge could be used to provide proof or disproof of a mixture rule, allowing for predictions of the dielectric strength of relevant battery vent gas mixtures by only performing measurements on the constituent gases. This would in turn facilitate making predictions of how vent gases from different battery chemistries under abuse would react in high-voltage environments, which could be valuable in battery design to avoid ignition. There are several battery chemistries under investigation both in industry and academia. Easily attainable predictions could be of value in the selection of suitable chemistries for study and use, for the advancement of the development of lithium-ion vehicle batteries. Moreover, it would be interesting to conduct further experiments with non-uniform electric fields as well, as it more closely resembles the operational environment of real battery packs. Such experiments could be performed using a similar setup to the one used in this thesis but with different electrode profiles.

Regarding the OH distribution measurements, the experimental results are in agreement with the trends shown in the simulations. Together, the trends shown in experiments and simulations indicate that the combustion at rich conditions is driven by H radicals. Such combustion processes can progress despite a very low oxygen supply, which means that fire could sustain even inside the battery pack and not only in contact with the surrounding air. This knowledge could be valuable in designing ways to quench the fire in case ignition occurs. Other battery vent gas mixtures could be of interest in the future, and these could be studied with a similar PLIF setup as used in this work. In this study, the OH radical was the focus but PLIF could also be performed on other radicals. If OH is studied together with the same discharge setup as in this work, structured light is not required to distinguish the emission from the OH from that of the discharge. If other discharge setups are used or other radicals are studied, structured illumination could be a suitable technique. Lastly, it is encouraging to see a technique that historically has found many applications within combustion engines and turbines now finding new applications related to studies of electrical vehicle batteries.

Now to a final conclusion connecting back to the schematic illustration of the problem scope in Figure 1.1. It has been demonstrated that the two experiment sets performed in this thesis have provided indicative results as well as directions and suggestions for further research on the two selected steps. The work in this thesis is to be considered a prestudy providing a roadmap to further investigations.

Bibliography

[1] Elna JK Nilsson, Christian Brackmann, and Annika Ahlberg Tidblad. "Evaluation of combustion properties of vent gases from Li-ion batteries". Under review for publication in *Journal of Power Sources* (2023).

[2] Arman Ahamed Subash and Elna Heimdal Nilsson. *Arcing as the ignition source in malfunctioning batteries*. Project report for Swedish Electromobility Centre, 2023. URL: https://emobilitycentre.se/.

[3] Jianan Zhang et al. "An Overview on Thermal Safety Issues of Lithium-ion Batteries for Electric Vehicle Application". *IEEE Access* 6 (2018), 23848–23863. DOI: https://doi.org/10.1109/ACCESS.2018.2824838.

[4] Qingsong Wang et al. "A review of lithium ion battery failure mechanisms and fire prevention strategies". *Progress in Energy and Combustion Science* 73.0360–1285 (2019), 95–131. DOI: https://doi.org/10.1016/j.pecs.2019.03.002.

[5] Xuning Feng et al. "Thermal runaway mechanism of lithium ion battery for electric vehicles: A review". *Energy Storage Materials* 10.2405–8297 (2018), 246–267. DOI: https://doi.org/10.1016/j.ensm.2017.05.013.

[6] Lingchen Kong, Yu Li, and Wei Feng. "Strategies to Solve Lithium Battery Thermal Runaway: From Mechanism to Modification". *Electrochemical Energy Reviews* 4.4 (2021), 633–679. DOI: https://doi.org/10.1007/s41918-021-00109-3.

[7] Languang Lu et al. "A review on the key issues for lithium-ion battery management in electric vehicles". *Journal of Power Sources* 226.0378–7753 (2013), 272–288. DOI: https://doi.org/10.1016/j.jpowsour.2012.10.060.

[8] Yuqing Chen et al. "A review of lithium-ion battery safety concerns: The issues, strategies, and testing standards". *Journal of Energy Chemistry* 59.2095–4956 (2021), 83–99. DOI: https://doi.org/10.1016/j.jechem.2020.10.017.

[9] M. Henriksen et al. "Laminar burning velocity of gases vented from failed Li-ion batteries". *Journal of Power Sources* 506.0378-7753 (2021), 230141. DOI: https://doi.org/10.1016/j.jpowsour.2021.230141.

[10] Michael Lammer, Alexander Königseder, and Viktor Hacker. "Holistic methodology for characterisation of the thermally induced failure of commercially available 18650 lithium ion cells". *RSC Advances* 7 (39 2017), 24425–24429. DOI: `https://doi.org/10.1039/C7RA02635H`.

[11] Andrey W. Golubkov et al. "Thermal runaway of commercial 18650 Li-ion batteries with LFP and NCA cathodes – impact of state of charge and overcharge". *RSC Advances* 5 (70 2015), 57171–57186. DOI: `https://doi.org/10.1039/C5RA05897J`.

[12] Alexander Petersson. Master's thesis, Lund University, 2023.

[13] Yuri P. Raizer. *Gas Discharge Physics*. Ed. by John E. Allen. Springer-Verlag Berlin Heidelberg, 1991. ISBN: 3-540-19462-2.

[14] Yangyang Fu et al. "Electrical breakdown from macro to micro/nano scales: a tutorial and a review of the state of the art". *Plasma Research Express* 2.1 (2020), 013001. DOI: `https://doi.org/10.1088/2516-1067/ab6c84`.

[15] P. J. Chantry and R. E. Wootton. "A critique of methods for calculating the dielectric strength of gas mixtures". *Journal of Applied Physics* 52 (1981), 2731–2739. DOI: `https://doi.org/10.1063/1.329081`.

[16] Huseyin R. Hiziroglu, Xingming Bian, and Tiebing Lu. "Experimental Study of Synergism in N2 and SF6 Gas Mixtures". *2020 IEEE 3rd International Conference on Dielectrics (ICD)* (2020), 814–817. DOI: `https://doi.org/10.1109/ICD46958.2020.9342004`.

[17] Predrag Osmokrović et al. "Synergistic effect of SF6 and N2 gas mixtures on the dynamics of electrical breakdown". *IEEE Transactions on Dielectrics and Electrical Insulation* 19.2 (2012), 677–688. DOI: `https://doi.org/10.1109/TDEI.2012.6180263`.

[18] Eva Oettinger, Malte Hildebrandt, and Bernhard Schmidt. "Electron drift velocity and Townsend coefficient in DME-based gas mixtures". *Nuclear Instruments and Methods in Physics Research Section A: Accelerators, Spectrometers, Detectors and Associated Equipment* 412.2–3 (1998), 355–360. DOI: `https://doi.org/10.1016/S0168-9002(98)00349-0`.

[19] L. Ledernez, F. Olcaytug, and G. Urban. "Inter-Electrode Distance and Breakdown Voltage in Low Pressure Argon Discharges". *Contributions to Plasma Physics* 52.4 (2012), 276–282. DOI: `https://doi.org/10.1002/ctpp.201100053`.

[20] Boya Zhang et al. "Evaluating the Dielectric Strength of Promising SF6 Alternatives by DFT Calculations and DC Breakdown Tests". *IEEE Transactions on Dielectrics and Electrical Insulation* 27.4 (2020), 1187–1194. DOI: `https://doi.org/10.1109/TDEI.2020.008906`.

[21] H.E. Nechmi et al. "Effective ionization coefficients and limiting field strength of fluoronitriles-CO2 mixtures". *IEEE Transactions on Dielectrics and Electrical Insulation* 24.2 (2017), 886–892. DOI: `https://doi.org/10.1109/TDEI.2017.006538`.

[22] Vinod Kumar Gandi et al. “Effect of Electrode Profile and Polarity on Performance of Pressurized Sparkgap Switch”. *Plasma* 5.1 (2022), 130–145. DOI: https://doi.org/10.3390/plasma5010010.

[23] F.M. Bruce. “Calibration of uniform-field spark-gaps for high-voltage measurement at power frequencies”. *Journal of the Institution of Electrical Engineers - Part II: Power Engineering* 94.38 (1947), 138–149. DOI: https://doi.org/10.1049/ji-2.1947.0052.

[24] W. Rogowski. “Die elektrische Festigkeit am Rande des Plattenkondensators”. *Archiv f. Elektrotechnik* 12.1 (1923), 1–15. DOI: https://doi.org/10.1007/BF01656573.

[25] N. Giao Trinh. “Electrode Design for Testing in Uniform Field Gaps”. *IEEE Transactions on Power Apparatus and Systems* PAS-99.3 (1980), 1235–1242. DOI: https://doi.org/10.1109/TPAS.1980.319754.

[26] Alan C. Eckbreth. *Laser Diagnostics for Combustion Temperature and Species*. 2nd ed. Vol. 3. Combustion Science and Technology Book Series. CRC Press, 1996. ISBN: 978-9056995324. DOI: https://doi.org/10.1201/9781003077251.

[27] Irvin Glassman, Richard A. Yetter, and Nick G. Glumac. *Combustion (Fifth Edition)*. Ed. by Irvin Glassman, Richard A. Yetter, and Nick G. Glumac. Fifth Edition. Academic Press, 2014. ISBN: 978-0-12-407913-7. DOI: https://doi.org/10.1016/B978-0-12-407913-7.00004-9.

[28] Xue-Song Bai. *Turbulent Combustion*. Lecture notes for the course *Turbulent Combustion* (MVK135 and MVK130F) at Lunds Tekniska Högskola (LTH), 2008.

[29] Wolfgang Demtröder. *Laser Spectroscopy, Vol. 1: Basic Principles*. 4th ed. Vol. 1. Springer-Verlag Berlin Heidelberg, 2008. ISBN: 978-3-540-73418-5. DOI: https://doi.org/10.1007/978-3-540-73418-5.

[30] Ronald K. Hanson, R. Mitchell Spearrin, and Christopher S. Goldenstein. *Spectroscopy and Optical Diagnostics for Gases*. Springer International Publishing Switzerland, 2016. ISBN: 978-3-319-23251-5. DOI: https://doi.org/10.1007/978-3-319-23252-2.

[31] Yupan Bao. “Development of optical diagnostics of plasma-related phenomena and applications”. PhD thesis. Lund University, 2022. ISBN: 978-91-8039-158-0. URL: https://lup.lub.lu.se/record/6aa18c8d-4b8d-401b-94ea-e487b5dd2db7.

[32] Elias Kristensson. “Structured Laser Illumination Planar Imaging SLIPI Applications for Spray Diagnostics”. PhD thesis. Lund University, 2012. ISBN: 978-91-7473-269-6. URL: https://portal.research.lu.se/en/publications/structured-laser-illumination-planar-imaging-slipi-applications-f.

[33] Yupan Bao et al. “Single-shot 3D imaging of hydroxyl radicals in the vicinity of a gliding arc discharge”. *Plasma Sources Science and Technology* 30.4 (2021), 04LT04. DOI: https://doi.org/10.1088/1361-6595/abda9c.

[34] Elias Kristensson et al. “Stray light suppression in spectroscopy using periodic shadowing”. *Optics Express* 22.7 (2014), 7711–7721. DOI: `https://doi.org/10.1364/OE.22.007711`.

[35] ANSYS. *CHEMKIN-PRO 15151*. 2016.

A

Experimental Setup

This addendum, authored by Julia Lövgren and Alexander Petersson, is intended to provide readers with a fundamental understanding of the experimental setup used in the Enoch Thulin laboratories to execute both experiments detailed within this thesis report. The information included provides a detailed description of the setup as it pertains to the primary equipment, i.e., gas supply, power supply, electrode setup and major monitoring equipment used. It is crucial to know that this addendum does not include precautions taken to mitigate hazards within the lab, such as grounding wiring or laser protection. For safety precaution information, please see Appendix B.

The experimental work done by Alexander Petersson and Julia Lövgren in the Spring of 2023 builds on a pre-study setup completed by Arman Ahamed Subash, funded by the Swedish Electromobility Centre as seen in [2].

Overall Setup

This addendum does not include the cameras used to record the high-speed imaging and the OH-PLIF data, nor does it include any information about the laser or the optics used to form the laser sheet for the laser diagnostics. As the specs and setup for these specific pieces of equipment are particular to the individual application for which they were used, the information can be found in the main body of the individual reports produced by Alexander Petersson and Julia Lövgren. The rendering below in Figure A.1 shows the overall experimental setup.

Electrode Setup

We begin with the two electrodes between which discharge occurs. Each one is made from a rod of stainless steel mounted on a Teflon piece and has a round copper head with a cone-shaped tip. The dimensions of the head given in millimetres are as shown in Figure A.2.

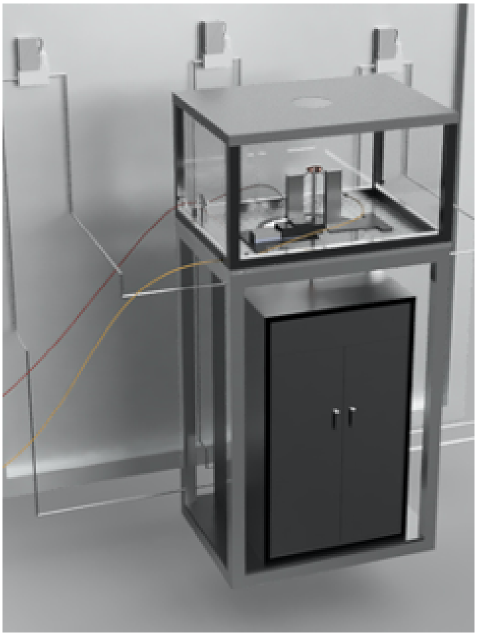

Figure A.1 A 3D model of the experimental setup in full.

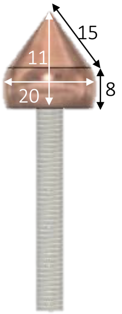

Figure A.2 Dimensions of a copper electrode head.

The electrodes are mounted so that the upper edges are approximately horizontal, ensuring that the smallest distance between the electrodes is between the tips and that the view of the discharge channel between the tips is not blocked by the electrode heads when viewed from the side. The electrode serving as the cathode is connected to the output of a power supply, while the electrode serving as the anode is connected to the ground of the power supply. The power supply delivers between 0-15 kV and 0-100 mA. The cathode electrode position is fixed, while the anode is placed on a translational stage allowing the distance between the electrode tips to be changed. In between the electrodes, a quartz tube is placed with its opening positioned 2.5 cm below the tips of the electrodes. Through this quartz tube, the gas medium is supplied through which discharge occurs. A 3D rendering of the setup as seen from the side is shown in Figure A.3 below. It is important to note that Figure A.3 does not depict safety measures taken, including grounding wires, rubber sheets, screws, or specific fittings such as bolts and washers.

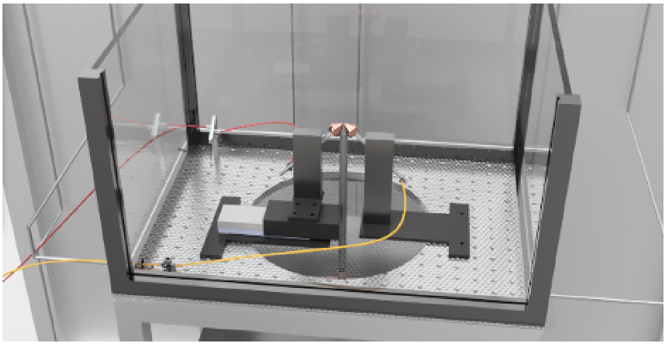

Figure A.3 3D rendering of the electrode setup and wiring.

Translational Electrode Stage for Cathode

One of the many significant requirements of the experiments performed in the present work is the ability to horizontally translate one electrode with great precision. It was decided that one electrode, the anode, would remain stationary while the cathode would have the ability to move horizontally. In order to do this, the Thor Labs MTS25 motorized translational stage was implemented. In combination with the provided Thor Labs attachable stage, the electrode was able to be mounted on top of the translational platform and could be precisely moved. The motor was controlled through a wired connection which implemented a graphical user interface from APT Software. Through this software, it was possible to move the electrode with precision in increments as small as 0.05 microns. In addition to providing the ability to move extremely small distances with great accuracy, the computerized control of the electrode minimized risk by eliminating the need to touch any equipment that had been exposed to dangerous amounts of electricity.

However, steps had to be taken to minimize the impact that the electromagnetic field from the high voltage would have on the functionality of this motor. To avoid any possible interference and minimize the amount of exposed metal near the electrodes, a "shield" was modelled and 3D printed to fit around the motor. This can be seen in the previous image, Figure A.3. It was also covered with aluminum foil, and a non-conductive, heat-resistant material to provide further protection.

Gas Supply

The gas medium is supplied to the quartz premixing tube via a three-line configuration as shown in Figure A.4, where flammable gas, oxidizer and heated inert gas were supplied separately. The quartz tube has an inner diameter of 9 mm and a length of 20 cm, providing optical access and electrical insulation from the electrodes. As previously mentioned, the distance from the electrode tips to the outlet of the quartz tube was 2.5 cm, which is considered to minimize surrounding air entrainment while still not having the electrodes severely obstructing the flow.

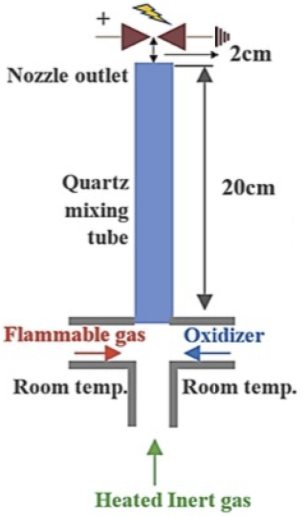

Figure A.4 Three-line gas flow configuration, schematic from [2].

The inert gas line passed through a furnace (Entech VSTF 50/11), providing the possibility of heating the inert gas. The flammable gas and oxidizer were injected as counterflows horizontally as shown in the sketch in Figure A.4, while the heated inert gas was injected vertically upwards through the quartz tube. The quartz tube is considered a preheat zone of the gas mixture resulting from the mixing of the three gases. The flammable gas and the oxidizer are at room temperature before mixing. The inert gas line and the oxidizer line are connected to the building's main gas supply lines, while the flammable gas line is connected to a high-pressure gas bottle. Upstream of the mixing point, each gas flows through a mass-flow controller (Bronkhorst El-Flow) allowing for precise volumetric flow rates to be specified. Upstream of each mass-flow controller, each line has a check valve preventing backflow toward the main gas supply or the high-pressure gas bottle. Additionally, there is a flame-quenching porous material at the base of the quartz tube to prevent excessive upstream propagation of the flame in the case of flashback.

Power Supply

The power supply consisted of two separate modules combining to deliver up to 16kV and 0-100mA. This power supply utilized a control module from Technix, designed to charge the capacitor bank and provide a front panel interface for controlling voltage and current settings. The capacitor bank used in this experiment was constructed in-house at the Enoch Thulin laboratories and has been used reliably within the combustion physics department at Lund University for a number of experiments. It is worth noting that this is the same power supply used in the pre-study [2], and therefore electrical inputs can be considered to be consistent in that aspect. Figure A.5 below is a photograph of the capacitor bank designed to provide the high voltage required to initiate an electrical discharge between the electrodes.

Current and Voltage Probes

A significant aspect of the experiment is the necessity to accurately measure the current and voltage at the point at which the electrical discharge occurs. For this, current and voltage probes were placed inside of the enclosed area and wired to an oscilloscope. Figure A.6 below shows the placement and wiring of the experimental setup when the probes were in use.

The oscilloscope used to measure the signals from the probes was a Teledyne Lecroy Wavesurfer 3054Z, capable of 500MHz across 4 different channels. For this experiment, only 2 channels were used. In order to protect the oscilloscope from the potentially damaging signal levels, 33 dB of attenuation was used on the channel measuring current. It is also important to note that the current probe output a signal of 1 volt per ampere measured.

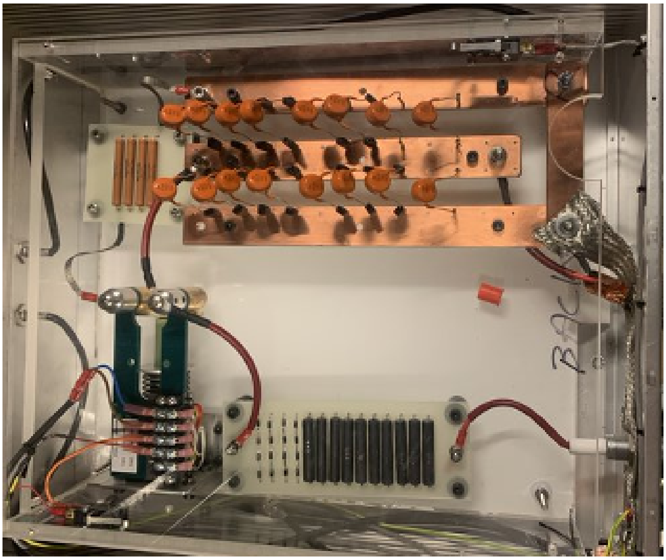

Figure A.5 Capacitor bank used for 16 kV power supply.

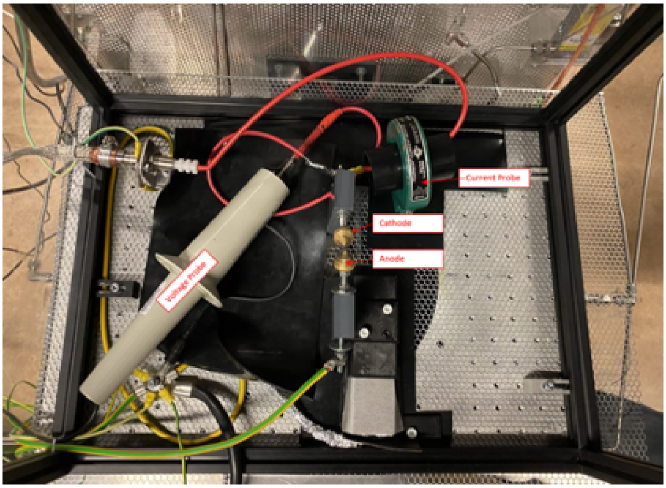

Figure A.6 Experimental setup with voltage and current probes viewed from above.

B

Risk Assessment of the Experimental Setup

The following document is a risk assessment of the setup described in Appendix A, authored by Julia Lövgren and Alexander Petersson.

Three main areas of risk have been identified. These are hazards regarding the electrical discharge and electrical circuits used to generate it, explosion and other risks related to gases, and hazards regarding the use of lasers for diagnostics. Measures to take in order to mitigate the risks related to these hazards are suggested here, as a complement to the working procedures in place at the Division of Combustion Physics, Lund University.

Electrical Hazards

- Short circuits can cause fires and electrical shock.
- High voltage may cause shock.
- Unintended sparks may ignite flammable material and gases.
- Electricity used within EX zones has explosion risks.
- The SS IEC Standard states that currents above 50 mA present a risk of potentially lethal heart fibrillation and burn injury. We work with 500 A and high voltage power supply.

In order to minimize electrical hazards and the risk of electrocution, steps have been taken to ground areas within the testing zone. Additionally, the following precautions should be taken to avoid adding unnecessary risk:

- Avoid extra materials within the testing area, such as liquids, books, pencils, etc. Any tools or equipment that may be needed within the test area should have non-conducting material for the handle.

- If inspection of the setup is needed, ensure power is disconnected.
- Keep electrical connections and switches clear. Ensure any new wiring is capable of accommodating active current before addition to the setup.

Gas and Explosion Hazards

- The laboratory contains storage of combustible gases, permanent gas lines, fuel storage, ventilation and working benches where combustible gas is handled which are EX-classed as risk zones (for explosion hazards), thus posing a risk especially together with electronic equipment. Within these zones, ignition sources are not allowed, including electrical equipment.
- Handling of gas cylinders, regulators and piping.
- Health hazards related to gases include suffocation from low oxygen levels and poisoning from toxic gases. If the oxygen level in the breathing air (normally at 21%) is at 15%, you feel weak, at 13% you feel exhausted and at 10 % you have fainted.
- Flammable gases pose a risk of fire.
- Pressurized vessels of gas constitute an explosion risk.
- Condensed gases are kept at low temperatures, causing a risk of freezing injuries.
- Risk of gas lines not being resistant enough for their contents, or not suited for the pressure and temperature at which they are used.
- Power failure, causing ventilation loss. See above the risks regarding combustible and health hazardous gases.

The following precautions should be taken to avoid adding unnecessary risk:

- Due to the intentional ignition of combustible gases, flame containment is critical to avoid possible propagation of flame upstream toward the gas storage. A porous quenching mesh at the inlet of the mixing area provides one source of protection, while check valves in each flow line provide another.
- Become familiar with all sources of gas flow. Ensure flow is completely cut off when testing is completed, and there is no obstruction in any of the flow paths.
- Become familiar with fire extinguishers, including when and how to use. Ensure they are properly maintained and accessible. Restrict extra materials on top of testing “cage”, specifically flammable materials.
- Ensure the ventilation system is unobstructed and ready to be used.

- Flammable gases are to be kept in the specified area. Do not put any possible sources of ignition in or around this area, and ensure proper maintenance of gas containers (no leaks or dents) and gas lines.

Hazards when Using Lasers

- Harm to eyes and skin.
- Class 3B lasers may cause harm to the eyes and minor skin injuries, while class 4 lasers are harmful to the eyes both by direct viewing and by viewing of diffuse reflections from surfaces. Class 4 lasers are also harmful to the skin.
- Both class 3B and class 4 lasers pose a risk of fire.
- Damage to the skin may consist of both burn wounds (thermal damage) and photochemical damage, as well as skin cancer from repeated exposure.
- Injuries from lasers depend on both the dose of radiation and on the wavelength.
- The blink reflex of the eyes may protect the eyes to some extent from visible light. Extra caution is needed when using ultraviolet lasers since they do not trigger the reflex.

The following precautions should be taken to avoid adding unnecessary risk:

- Use appropriate eye protection when lasers are in use if necessary. Laser operation in this laboratory should be able to be performed without being in the area of the laser, so avoiding the area during laser use altogether would minimize risk.
- Ensure the testing area is clear of extra materials that may interfere with laser diagnostics, can diffuse or reflect lasers, or be damaged by lasers.
- Become familiar with the control of the laser system. If applicable, understand when and how to use a disconnect switch to manually deactivate the laser.
- To minimize risk in all areas mentioned in this document, unauthorized persons should not be permitted in the lab during operation.

C

Breakdown Current Plots

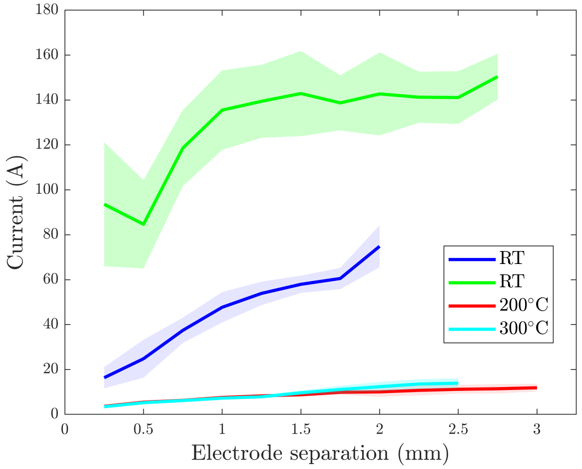

Figure C.1 Current in N_2 at a flow velocity of 5 m/s. Two measurement series are included for room temperature (RT).

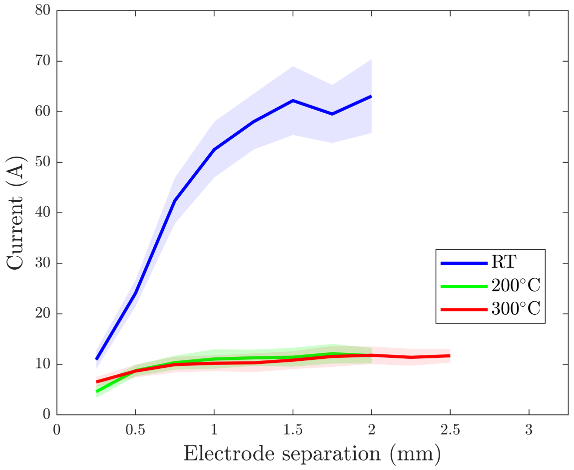

Figure C.2 Current in LFP at a flow velocity of 5 m/s. RT represents room temperature.

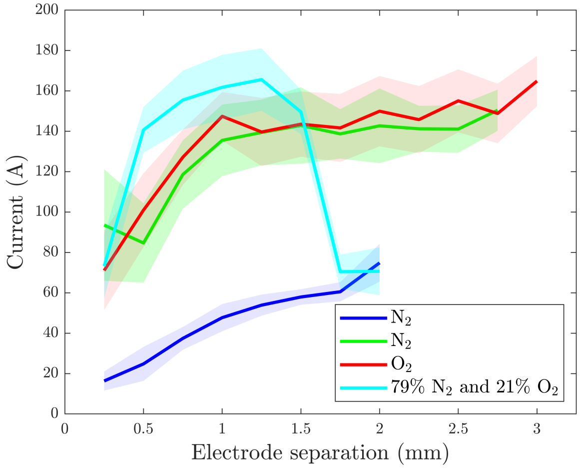

Figure C.3 Current in N_2, O_2 and a mixture of the two at room temperature and a flow velocity of 5 m/s. Two measurement series are included for N_2.

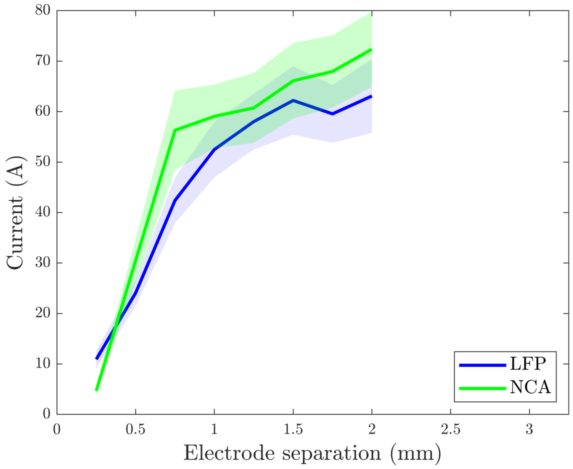

Figure C.4 Current in the two gas mictures at room temperature and a flow velocity of 5 m/s.

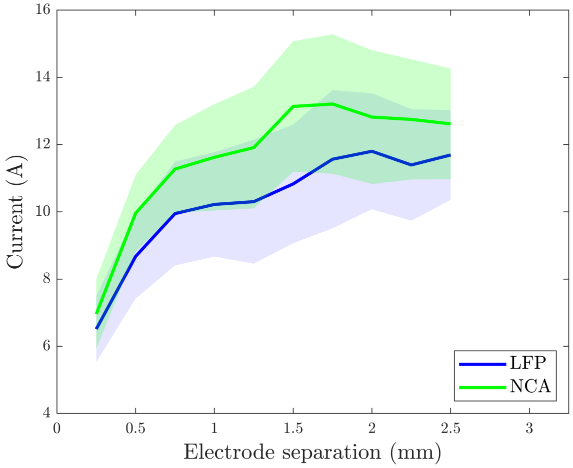

Figure C.5 Current in the two gas mictures at 300°C and a flow velocity of 5 m/s.

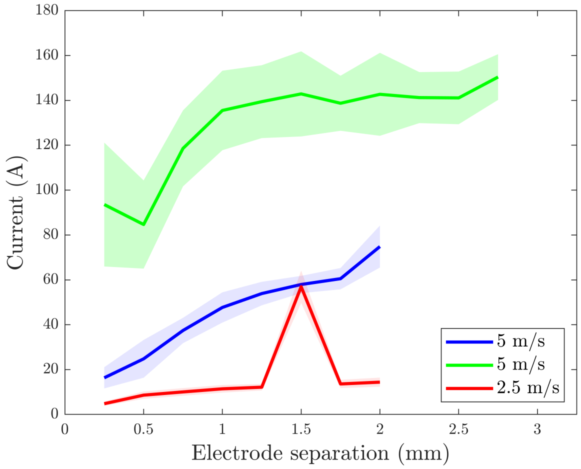

Figure C.6 Current in N_2 at different flow velocities at room temperature. Two measurement series are included for 5 m/s.

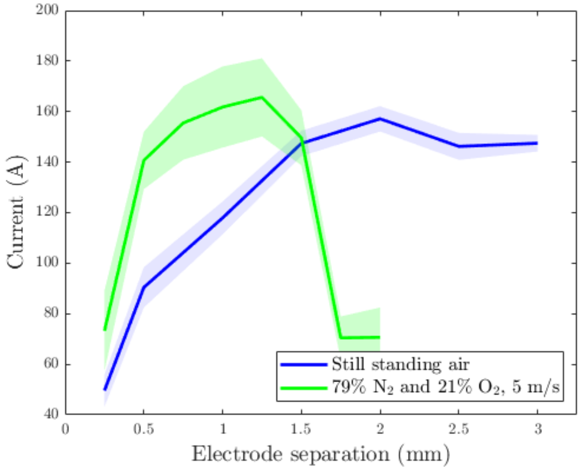

Figure C.7 Current in still standing air and in a mixture of 79% N_2 and 21% O_2 at a flow velocity of 5 m/s, measured in room temperature.